



Plateau–Rayleigh instability in a capillary: assessing the importance of inertia

Matthieu Rykner¹, Elie Saikali¹, Adrien Bruneton¹, Benoît Mathieu² and Vadim S. Nikolayev^{3,†}

¹Université Paris-Saclay, CEA, Service de Génie Logiciel pour la Simulation, 91191 Gif-sur-Yvette, France

²Université Grenoble Alpes, CEA Liten, 38054 Grenoble, France

³Université Paris-Saclay, CEA, CNRS, Service de Physique de l'Etat Condensé, 91191 Gif-sur-Yvette Cedex, France

(Received 29 April 2024; revised 26 July 2024; accepted 12 August 2024)

Liquid plug formation in thin channels due to the Plateau–Rayleigh instability of a liquid film is observed in a variety of fields. In this paper, complementarity between theoretical solutions and direct numerical simulations (DNS) based on a front-tracking algorithm is explored to evaluate the importance of inertia for the case of a cylindrical capillary. A linear stability analysis is first performed and DNS results are then used to investigate the spatial distributions of inertial, convective and viscous terms of the Navier–Stokes equation. The existence of both viscous and inertial regimes is evidenced with a threshold given by the film thickness. The presence of the core fluid slows down the instability. In the viscous regime, predictions of the lubrication theory are verified. An example of liquid water as the outer fluid film and water vapour as the inner core fluid is simulated with application to the fuel cells.

Key words: computational methods, capillary flows

1. Introduction

Two-phase flows in capillary tubes are encountered in a variety of natural and industrial processes. Despite the consequent number of studies devoted to this field, their behaviour is still difficult to predict. Among the challenges is the correct understanding and prediction of the channel occlusion phenomenon, i.e. transition between the annular regime where a liquid film covers the channel walls and the plug regime where liquid obstructs the channel. Occlusion of micrometric channels is notably observed in porous

† Email address for correspondence: vadim.nikolayev@cea.fr

media related problems, such as oil recovery (Gauglitz & Radke 1990; Beresnev, Li & Vigil 2009) or carbon storage (Deng, Cardenas & Bennett 2014), in microfluidic applications (Günther *et al.* 2004) or in medical applications. Ample studies have notably been devoted to the understanding of lung airway closure, a phenomenon responsible for diseases such as pulmonary edema, asthma, emphysema or respiratory distress syndrome (Halpern *et al.* 2008). Airway occlusion studies have been able to integrate key aspects such as airway wall elasticity (Halpern & Grotberg 1992; Rosenzweig & Jensen 2002; Hazel & Heil 2005), surfactant effects (Halpern, Jensen & Grotberg 1998; Romanò, Muradoglu & Grotberg 2022) or visco-elastic and visco-plastic properties of the liquid film layers (Romanò *et al.* 2021; Erken *et al.* 2023). While studies have assessed the importance of inertia in lungs (Fujioka & Grotberg 2004) and have demonstrated it can be significant in large airways and negligible in smaller ones, the fluid properties and the issues at stake in that field strongly differ from that of other fields such as fuel cells, where channel occlusion is also observed (Lu *et al.* 2011; Cheah, Kevrekidis & Benziger 2013).

Proton exchange membrane fuel cells (PEMFC) is one of the promising technologies that can be used to decarbonise and electrify the energy system. Electricity is produced by recombining oxygen and hydrogen that are fed via millimetric gas flow channels (GFCs) at the two opposite sides of the cell. The operating pressure in GFCs is 1–2 bar. A porous media, the gas diffusion layer, separates the GFCs from a central membrane, on the surface of which two catalyst layers are deposited. All chemical reactions occur on these catalyst layers usually composed of carbon–platinum particles. As it operates at rather low temperatures (60–80 °C), water can be observed both as liquid and vapour, creating a two-phase flow in the GFCs. Formation of plugs has been experimentally evidenced in GFCs both in *ex-situ* (Lu *et al.* 2011) and *in-situ* (Hussaini & Wang 2009) studies. While the GFCs will be modelled in a simplified way in this paper, they have in reality a much more complex geometry and are subject to a number of physical phenomena (thermal effects, gas composition changes) outside the scope of this paper.

Considering all these complexities, fully analytical solutions seem insufficient to predict and manage water evolution in a fuel cell. However, numerical simulations based on computational fluid dynamics (CFD) methods are able to simulate these complex phenomena, at the cost of being expensive and requiring validation. This study aims at demonstrating the relevance and complementarity of numerical and analytical methods. Relying on both techniques, the role of inertia in the formation of plugs in fuel cell conditions will be assessed, thus allowing a deeper understanding of two-phase flow in fuel cells. In the following introduction we proceed with a description of the plug formation phenomenon and the main approaches to investigate it.

Plug formation is primarily caused by the Plateau–Rayleigh instability, first experimentally evidenced by Plateau (1873). Subject to surface tension forces, a film of fluid covering the interior of a tube can be unstable. For a given volume of fluid, the film tends to minimise its surface energy by deformation, which can eventually lead to plug formation. One of the key aspects of the Plateau–Rayleigh instability is the competition between the two components of the film curvature. The film is destabilised by its radial component and stabilised by its axial one. As a consequence, the plug periodicity is proportional to the initial radius of the fluid interface. Another consequence of the Plateau–Rayleigh instability is the breakup of fluid jets into droplets, which has been thoroughly investigated by Rayleigh (1878). Rayleigh (1878) also developed the mathematical framework for the linear regime of the instability; this work was later pursued by Weber (1931), Tomotika (1935) and Christiansen & Hixson (1957). A good summary of these models can be found in Lee & Flumerfelt (1981). The theory of jet

breakup was later adapted to the breakup of a film covering the interior or exterior of capillaries by Goren (1962), but only considering the film fluid. All these pioneering works are however limited to a linear stability analysis.

Based on a purely static analysis, Everett & Haynes (1972) demonstrated that under a critical value of the film thickness, its breakup is impossible due to volume limitations. In that case, liquid plugs are replaced by unduloid shapes (called collars by other authors) that do not obstruct the capillary. This prediction was confirmed by their experiments. Hammond (1983) proposed a nonlinear lubrication model, where the flow is assumed laminar, inertialess and fully developed and where the radial scale is small compared with the axial scale. His model leads to the formation of collars, whose long-term evolution was studied, notably predicting the apparition and subsequent drainage of secondary local maxima called satellite lobes. Nevertheless, his model does not lead to plugs for thick films, contradicting the Plateau–Rayleigh theory. Gauglitz & Radke (1988) used a better estimate of the curvature, still within the lubrication approach. By numerically solving their model, they obtained a critical thickness value separating collar and plug regimes, that was partially confirmed by their experiments. More recently, Lister *et al.* (2006a) pursued Hammond (1983) study of the long-term evolution of stable collars. They predicted the possibility for satellite lobes to exhibit back-and-forth sliding motion between adjacent collars.

All the previous lubrication developments neglected the effects of both the core fluid and inertia. Most of the studies attempting to take into account the core fluid were focused on the effect of an imposed core flow. As first demonstrated by Frenkel *et al.* (1987) this flow can prevent channel occlusion. These effects were studied either within the thin film approximation (Frenkel *et al.* 1987; Papageorgiou, Maldarelli & Rumschitzki 1990; Kerchman 1995) or within the frozen-surface approximation (Halpern & Grotberg 2003; Camassa, Ogrosky & Olander 2017) where the outer liquid velocity is assumed negligible compared with the core gas one. In the frozen-surface approximation the core gas sees the interface as a rigid wall. It is also worth noting the work of Hickox (1971) who highlighted the existence of another instability arising from the viscosity difference between the inner and outer fluids when an external flow is imposed (either due to gravity or to an imposed pressure gradient). Hickox (1971) demonstrated that a Poiseuille two-phase flow is always linearly unstable, although he predicted that it can be stabilised by nonlinear effects in the form of a wave-propagating state, as later confirmed by Frenkel *et al.* (1987). In the absence of an imposed core flow, only a few studies integrated the effect of the core fluid. This was notably done by Georgiou *et al.* (1991) in a linear stability analysis of an electrolyte film-dielectric core system. When considering only mechanical properties of their liquid–liquid system, they highlighted the role of the viscosity ratio of the core and outer fluids, also considering inertia, yet assuming identical densities for both fluids.

Including inertial effects outside the linear regime is much trickier, but is achievable by using integral methods or long-wave expansion techniques. Integral models are based on the integration of the Navier–Stokes equations over the tube cross-section. Johnson *et al.* (1991) were the first ones to use an integral method to obtain a film evolution equation. They however needed to prescribe base velocity profiles in their equations by using a constant (inviscid) profile for the inertia term and a Poiseuille (inertialess) profile for the viscosity term. These approximations restrict their model in the transition regime where both inertia and viscosity are significant. Recently, more sophisticated models were developed by Camassa, Ogrosky & Olander (2014) and Dietze & Ruyer-Quil (2015). Both models are based on a long-wave second-order expansion of the Navier–Stokes equations, including inertia and streamwise viscous diffusion. The flow is decomposed into a base

velocity, which is more consistent than that of Johnson *et al.* (1991), and higher-order corrections. The models differ on the handling of the correction velocities. While Camassa *et al.* (2014) derive each correction from the value of its smaller order, Dietze & Ruyer-Quil (2015) approach is based on the theory of Ruyer-Quil & Manneville (2002), where the Navier–Stokes equations are integrated over the channel cross-section. By choosing an appropriate set of tailored weights, it is possible to eliminate higher-order correction velocities. Such models require smaller computation times than CFD, so that the long-term behaviour can be studied similarly. Nevertheless, these models are restricted to relatively simple geometries and require significant analytical developments.

On the other hand, numerical simulations are more suitable for systems with complex geometry including numerous physical phenomena that apply either locally or on the whole domain (Magnini 2022). In the field of two-phase flows where the phases are clearly separated, CFD simulations are usually performed using direct numerical simulations (DNS). They provide a good resolution of the interface and do not require subgrid models. Nevertheless, they are computationally expensive, limiting their ability to provide results at long physical time. Direct numerical simulations in capillaries have been mostly focused on the displacement of already formed liquid plugs (Magnini *et al.* 2017). Few DNS were however focused on the development of the Plateau–Rayleigh instability in the absence of imposed flow. Johnson *et al.* (1991) used a spectral method to solve the Navier–Stokes equations coupled with an arbitrary-Lagrangian–Eulerian method to track the interface. They were able to reproduce the evolution of the film maximal thickness that they previously obtained from a nonlinear integral method. Based on a front-tracking approach coupling a fixed Eulerian volume mesh and a moving Lagrangian interfacial mesh, Tai *et al.* (2011) simulated the early stages of the instability. They obtained velocity fields and wall shear stress evolution that could be compared with the experimental data of Bian *et al.* (2010). By using the volume of fluid technique the same group was able to simulate the complete plug formation (Romanò *et al.* 2019). They demonstrated the existence of a peak in the wall shear stress and wall pressure gradient, right after channel occlusion. These studies aimed at improving the knowledge of the airway occlusion phenomenon and were later pursued to study the effects of visco-elasticity (Romanò *et al.* 2021) and the presence of surfactants (Romanò *et al.* 2022). However, the parameters used in these studies strongly differ from those observed in other systems of industrial importance, e.g. the liquid water/vapour system used in fuel cell channels. In particular, the role of inertia is negligible in the highly viscous outer fluid (mucus film in their case).

Experimental observations of the liquid plug formation proves very difficult as characteristic times and dimensions are small, specifically for the water liquid/vapour system. Hence, more viscous fluids were used in the experiments to increase the channel occlusion time. Liquid water is most often used for the core and more viscous silicone oil or glycerol is used for the outer (film) fluid. With such fluids, plug formation was observed early by Goldsmith & Mason (1963), with a good picture quality by using an ordinary reflex camera. However, their experiments were focused on centimetric channels (between 1 and 4 cm) where gravity can play a role. On the contrary, Aul & Olbricht (1990) replicated the same experiments on micrometric channels (50 μm). They were able to observe the formation of both liquid plugs and stable collars depending on the initial film thickness. More recently, with the help of micro-particle image velocimetry techniques, Bian *et al.* (2010) observed not only the interface evolution, but also the flow velocity distribution. Nevertheless, experimental studies are still limited by the camera resolution and the acquisition frequency. It is notably difficult to access small amplitude

Plateau–Rayleigh instability in a capillary

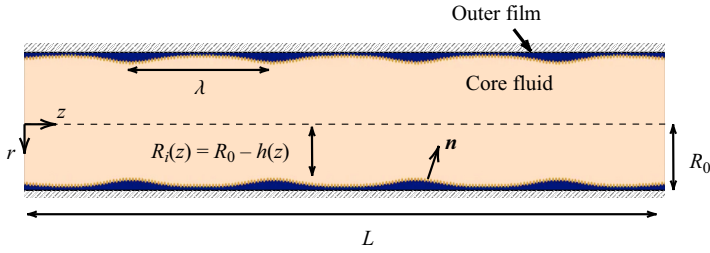


Figure 1. Sketch of the problem geometry.

perturbations present at the instability initiation. In this paper a numerical approach is chosen to more precisely capture its dynamics.

The goal pursued by the authors is to evaluate the role played by inertia in the Plateau–Rayleigh instability. We target the water liquid/vapour system to improve the understanding of its behaviour in the PEMFC channels. The paper is structured as follows. The physical problem is first detailed in § 2. After being introduced (§ 3), the numerical simulations are validated against well-known analytical and experimental results (§ 4). Next, they are used as a reference to examine the relative contributions of inertia, convection and viscous forces to the Plateau–Rayleigh instability, first through a linear stability analysis (§ 6) and then by spatially mapping these contributions (§ 7). The analytical models used in the result sections are introduced in § 5.

2. Physical problem

This paper focuses on the development of the Plateau–Rayleigh instability in a cylindrical capillary. The parameters are chosen to match those of typical PEMFC conditions. The capillary tube, illustrated by figure 1, has a radius $R_0 = 0.5$ mm and a length $L = 2$ cm. All models and simulations developed in this paper use axial symmetry.

The tube wall is completely covered by a thin film of fluid, usually liquid (water in PEMFC) denoted with the subscript l . It has an initial average thickness h_0 . This outer fluid surrounds a core fluid, usually a gas (water vapour in PEMFC), denoted with the subscript g , with the initial average core radius $R_i = R_0 - h_0$. As the tube is small in diameter, the Bond number $Bo = \rho_l g R_0^2 / \sigma$ is smaller than 0.05 for liquid water, so the gravitational effects can be neglected. Both fluids are assumed to be incompressible. Interfacial phase change and thermal effects are also neglected.

Seven physical parameters govern the dynamics of this system: shear viscosities μ_k , densities ρ_k ($k = l, g$), the surface tension σ , the tube radius R_0 and the film initial thickness h_0 . The physical parameters are assumed constant. In PEMFC conditions, their values are taken at a temperature of 100 °C (table 1). Water vapour is considered as the core gas; oxygen and nitrogen present in real PEMFC are ignored here. Such a fluid combination is used in subsequent sections unless otherwise specified. By scaling times by $R_i \mu_l / \sigma$, lengths by R_i and pressures by σ / R_i , one reduces the problem to four dimensionless parameters: the dimensionless initial film thickness ϵ , the viscosity ratio m , the outer fluid Laplace number J_l and its equivalent for the core fluid J_g . Such parameters were notably used by Georgiou *et al.* (1991):

$$\epsilon = \frac{h_0}{R_0}, \quad m = \frac{\mu_g}{\mu_l}, \quad J_l = \frac{\rho_l \sigma R_i}{\mu_l^2} \quad \text{and} \quad J_g = \frac{\rho_g \sigma R_i}{\mu_l^2}. \quad (2.1a-d)$$

Physical quantity	Value
μ_l	280 $\mu\text{Pa s}$
μ_g	12.3 $\mu\text{Pa s}$
ρ_l	958.4 kg m^{-3}
ρ_g	0.597 kg m^{-3}
σ	58.9 mN m^{-1}

Table 1. Physical values for the water vapour (core fluid, subscript g) and liquid water (outer fluid, subscript l) at saturation at 100 °C. These values were found with the CoolProp Python library (Bell *et al.* 2014).

It should be noted that the Laplace numbers J_l and J_g have been designed so that their ratio equals the density ratio. However, this implies that both Laplace numbers decrease with ϵ . While this is logical for J_g (the higher ϵ is, the less inertia will be significant in the core fluid), this does not represent the fact that, in the outer film, inertia actually increases compared with viscosity for a thicker film.

3. Numerical modelling and CFD software

3.1. Front-tracking method

The numerical study is performed using the open source TrioCFD software within the TRUST HPC platform (Calvin, Cueto & Emonot 2002; Saikali *et al.* 2021). Based on an object oriented design, the code is massively parallel and is written in modern C++ language.

A two-phase flow module, based on a discontinuous front-tracking (DFT) method (Mathieu 2003), is employed. In this method the interface between two fluid phases is defined as moving connected-marker points (Lagrangian grid), independent from the Eulerian grid used to mesh the computational domain. On the Eulerian mesh, one-fluid velocity and pressure fields are considered for both phases and updated by solving the Navier–Stokes equations. The markers of the moving Lagrangian grid are, for their part, advected by the velocity field of the Eulerian mesh as described in du Cluzeau, Bois & Toutant (2019). The phase indicator function, and thus, the physical properties of each phase (density and viscosity) are finally updated using the new marker positions.

The discretisation in space is performed by a mixed finite difference/volume method that is implemented on a staggered Eulerian grid of type marker and cell. Spatial derivatives are discretised with a classical second-order centred scheme.

A first order semi-implicit time integration scheme (matrix free) is employed where the diffusion terms are treated implicitly, while the convective terms are explicitly considered. As a consequence, the time step is dynamically selected at each iteration respecting the Courant–Friedrichs–Lewy (CFL) criterion, thus ensuring the stability of the numerical scheme. However, this criterion does not enforce stability for the Lagrangian grid motion and time steps must be limited by a maximum value, which needs to be chosen following a convergence study (§ 3.4). The linear system of equations resulting from the implicit treatment of the diffusion terms is solved (Saad 2003) by the conjugate gradient method (CGM). The library PETSc (2024) is used for this purpose.

To handle the velocity–pressure coupling, a projection method is used satisfying the mass conservation equation. The resulting elliptic pressure Poisson equation is solved with CGM and symmetric successive over-relaxation preconditioning. More technical details on the algorithm are given by Saikali (2018).

3.2. Governing equations for numerical treatment

The one-fluid equations of Kataoka (1986) solved by TrioCFD are

$$\nabla \cdot \mathbf{v} = 0, \quad (3.1)$$

$$\frac{\partial \rho \mathbf{v}}{\partial t} + \nabla \cdot (\rho \mathbf{v} \times \mathbf{v}) = -\nabla P + \nabla \cdot [\mu(\nabla \mathbf{v} + \nabla^T \mathbf{v})] + \sigma \kappa \mathbf{n} \delta^i, \quad (3.2)$$

where the one-fluid variables are obtained from their values in each phase: $\phi = \chi_g \phi_g + \chi_l \phi_l$ with ϕ_k either the velocity (\mathbf{v}_k), pressure (P_k), density (ρ_k) or viscosity (μ_k) of the fluid $k = l, g$. Here χ_k is the phase indicator function, equal to 1 in phase k and 0 elsewhere. The gas phase indicator χ_g is transported through $\partial \chi_g / \partial t + \mathbf{v}_i \cdot \nabla \chi_g = 0$, where $\mathbf{v}_i = \mathbf{v}(R_i)$ is the interfacial velocity. In the absence of phase change, the velocity is continuous across the interface. Here σ is the surface tension, $\kappa = -\nabla \cdot \mathbf{n}$ the local curvature and \mathbf{n} the interface normal directed towards the core fluid and defined by $\nabla \chi_l = -\mathbf{n} \delta^i$, where δ^i is the Dirac delta function centred at the interface.

3.3. Initial and boundary conditions

Boundary conditions are required for both the Eulerian fixed mesh (pressure or velocity) and the Lagrangian mesh (interface). For the former, zero velocities are imposed both at the wall (no-slip) and at the open boundaries (inlet/outlet). At the open boundaries the interface position is pinned at a user-defined position (the average initial film thickness h_0). This last boundary condition has been specifically developed for this study. Symmetry conditions (90° slope for the interface and zero derivative for the velocity field) are necessary on the symmetry axis.

The film is initialised as a sinusoidal perturbation around h_0 . The initial amplitude is chosen to be negligible compared with h_0 (between 1 and 5 μm depending on the simulation). The wavelength can be modified to cover the dispersion spectrum.

3.4. Mesh and convergence study

A convergence study is first performed on a small sample of cases to select a well-suited mesh and a correct maximum time step. One should note that the convergence of the front-tracking algorithm does not follow regular convergence laws. The time step choice is also a complex task as no reliable criterion (like CFL) exists for the interface remeshing algorithm. However, CFL criteria are used to determine the convection time step. It is hence necessary to test the DFT method for several maximum time step values until reaching convergence for each mesh.

One of the convergence studies is presented in figure 2. Two variables are chosen to evaluate the convergence: one related to the Lagrangian mesh (the characteristic time of destabilisation t_{destab} related to the speed of the instability) and one for the Eulerian mesh (the average velocity \bar{v} measured in the central part of the domain in the 10% physical time before channel occlusion). Except for the coarsest meshes, convergence in time step is achieved for all meshes. Moreover, errors smaller than 1% are obtained when the mesh is constituted of more than 200 000–400 000 cells. A mesh of 400 000 cells and a maximum time step 0.5 μm are thus chosen. The mesh is then refined close to the wall (on one tenth of the radius) with a hyperbolic tangent refinement, in order to be able to simulate thinner films and, thus, longer times. The mesh size is comprised between 0.5 μm close to the wall in the radial direction and 5 μm in the axial direction. It contains 488 000 cells. A zoom in on the mesh on a fraction of the tube is illustrated in figure 3, and the corresponding values

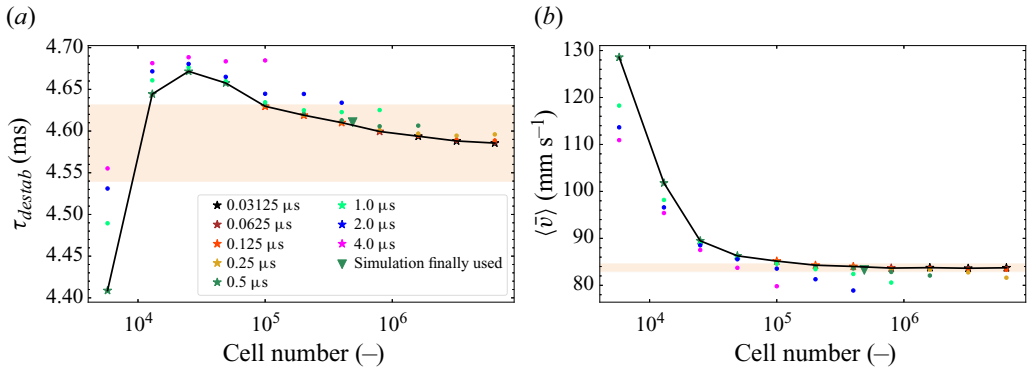


Figure 2. Mesh and time step convergence studies. Colours indicate the maximum time step. The smaller maximum time steps for each mesh are depicted by a star and linked together by the plain line. The triangle point is the value for the refined mesh finally used. The coloured area is the 1% zone around the converged value. (a) Characteristic time of destabilisation. (b) Average velocity.

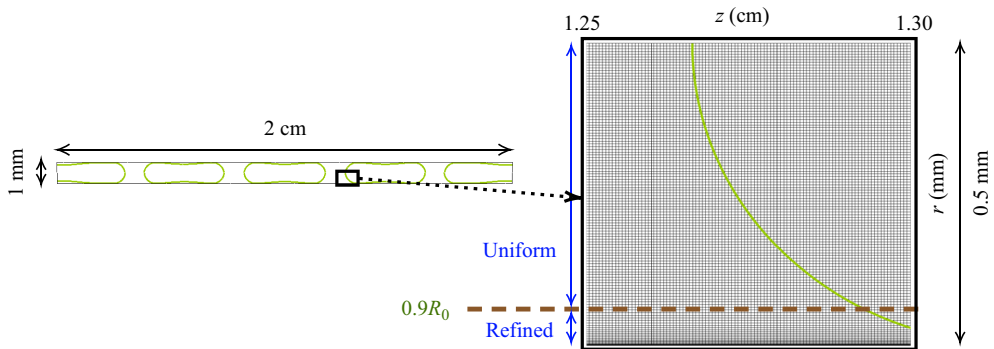


Figure 3. Locally refined DNS mesh. The interface is displayed in green.

of the convergence variables are reported in [figure 2](#) with triangles. As soon as the liquid film becomes thinner than 10 mesh cells, the results are discarded as being uncertain due to film sub-resolution.

The selected mesh and time step are rather conservative choices to ensure the best results. Although they are small, the computational cost is still reasonable. Nevertheless, coarser meshes and higher maximum time steps may be more reasonable choices for future studies, where longer domains and simulation times may be required.

4. Validation of DNS simulations

The DFT method used in TrioCFD was initially developed to study the behaviour of bubbles. It has not been tested for the particular case of a thin film with open boundaries. A validation of this method is thus performed with respect to both analytical and experimental results.

4.1. Collar-plug transition

Results of two simulations, for $\epsilon = 0.1$ and 0.2 , are presented in [figure 4](#). The parameters from [table 1](#) are used. Although for a sufficiently thick film the Plateau-Rayleigh

Plateau–Rayleigh instability in a capillary

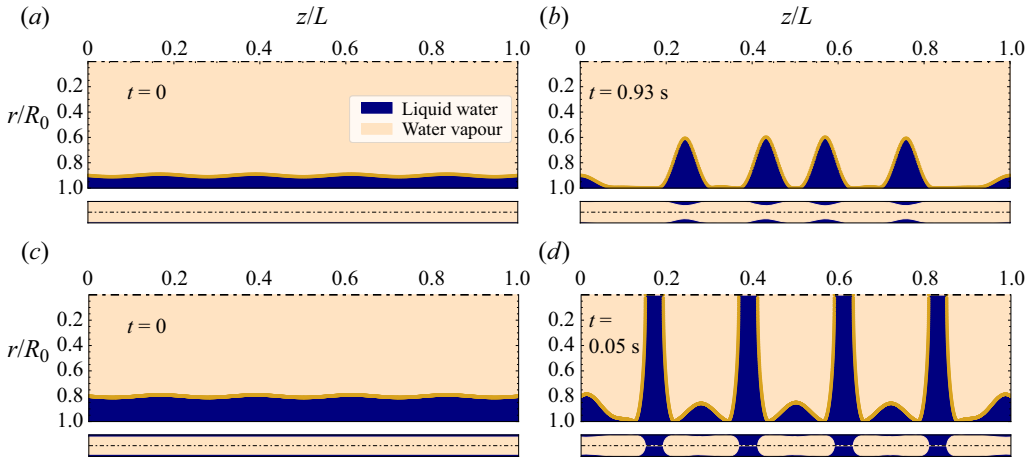


Figure 4. Initial (*a,c*) and final (*b,d*) phase distributions inside a capillary caused by the Plateau–Rayleigh instability for $\epsilon = 0.1$ (*a,b*) and $\epsilon = 0.2$ (*c,d*), cf. supplementary movies available at <https://doi.org/10.1017/jfm.2024.1024>. The lower figures show the channel with the actual aspect ratio.

instability causes the formation of plugs, thin films are not able to completely clog it. Instead, they form stable collars that do not attain the tube axis and obstruct the tube only partially. Indeed, as predicted by Everett & Haynes (1972), for a given volume of liquid, plugs alone (for large volumes), collars alone (small volumes) or a co-existence of both of them can occur. No collars can exist for volumes higher than $\simeq 1.74\pi R_0^3$, which corresponds to a critical value ϵ_{cr} of the thickness close to 0.0980. Everett & Haynes (1972) also pointed out that one of these two configurations (collar or plug) is favoured, having a smaller effective interface area or interfacial energy. A hysteresis (i.e. collar/plug coexistence) is thus possible and plugs may exist for $\epsilon \sim 0.04$. In the present case, as simulations always start from a nearly flat film shape (unduloid with vanishing eccentricity), this hysteresis cannot be investigated and the study is restricted to the collar configuration if it exists, to the plug configuration otherwise.

Although, in a thin film approximation, only collar shapes can be observed (Hammond 1983), Gauglitz & Radke (1988) developed a lubrication model to capture the collar-plug transition, finding $\epsilon_{cr} \simeq 0.12$. They also compared their predictions to experiments, in which the threshold value was rather 0.09. They explained this discrepancy by the coalescence of neighbouring collars, that they expect to be responsible of secondary plug formation for $0.09 \leq \epsilon < 0.12$.

In the present simulations, collars are observed for $\epsilon < 0.12$, which agrees with Gauglitz & Radke (1988). However, secondary coalescence of collars could not be simulated due to mesh resolution limitations when the liquid film between collars thins. When its thickness decreases below 5–10 cells (which eventually occurs for $\epsilon \leq 0.11$) the simulation is considered to be invalid. However, it is possible to observe neighbouring collars getting closer for $\epsilon = 0.1$ and 0.11 (figure 4*b*) that is not yet observed for smaller ϵ . Such a process can eventually lead to their coalescence. Hence, DNS agrees well both with the theory and the experiments of Gauglitz & Radke (1988). Compared with the Everett & Haynes (1972) results, our numerical value is slightly higher than their prediction, which is most probably linked to the existence of satellite lobes between neighbouring collars/plugs. These smaller satellite lobes can retain a significant volume of fluid, which becomes unavailable for the main collar. The static critical thickness is probably underestimating its dynamic value,

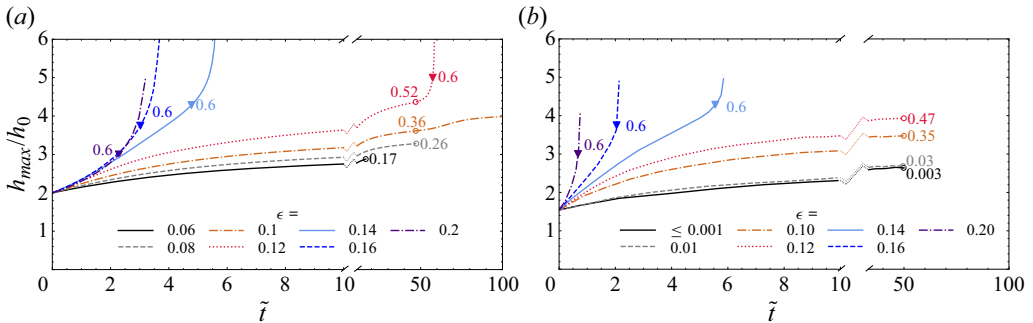


Figure 5. Evolution of the maximum film thickness $h_{max}(t)$ for different ϵ . (a) Direct numerical simulation results. (b) Results of Gauglitz & Radke (1988). Triangles indicate the times where $h_{max}/R_0 = 0.6$ and circle points indicate particular states with corresponding values of h_{max}/R_0 . If stable collars are formed, the final value of h_{max}/R_0 is indicated. Time scaling $\tilde{t} = t\sigma\epsilon^3/(3\mu_l R_0)$ follows that of Gauglitz & Radke (1988).

although the long-term behaviour of static collars is not perfectly accessible in these simulations.

The dynamics of the collar growth was also obtained by Gauglitz & Radke (1988) with their lubrication model. For the DFT validation, their results (figure 5b) are reproduced using DNS in figure 5(a). The time evolution of the maximum film thickness h_{max} in the central part of the simulation domain is plotted for different ϵ . Because velocities are initialised at zero in DNS, some time is needed to reach a well-established regime. To obtain comparable plots, we choose $t^* = 0$ when h_{max} reaches $2h_0$ in figure 5(a). All the curves first exhibit an exponential increase. As experimentally observed by Goldsmith & Mason (1963), an acceleration occurs next for thick films (in blue) that eventually form plugs. It is due to the cylindrical geometry: for the same change of h , the volume that needs to be filled to form a plug is reduced as h_{max} grows. As predicted by Gauglitz & Radke (1988), this acceleration starts when $h_{max} \simeq 0.6R_0$. These points are indicated by triangles in figure 5. On the contrary, for thin films, the interface decelerates. It then asymptotically reaches the stable collar state of figure 4(b) shown with circle characters. Finally, the films of initial thickness slightly higher than ϵ_{cr} can first exhibit a deceleration and then an acceleration. Figure 5(a,b) agrees very well, validating the DNS simulations on this particular metric. Notably, collar thickness values are identical for similar cases. The main difference is the behaviour for $\epsilon = 0.12 \approx \epsilon_{cr}$ where the channel becomes clogged in our DNS but not in the simulations of Gauglitz & Radke (1988) that were probably not long enough. Similarly, case $\epsilon = 0.10$ exhibits a sliding motion at long times, which slightly increases h_{max} .

4.2. Velocity profiles and wall shear stress

Velocity profiles of the channel occlusion phenomenon were obtained both with particle image velocimetry measurements (Bian *et al.* 2010), numerically solved analytical models (Johnson *et al.* 1991) and DNS (Tai *et al.* 2011; Romanò *et al.* 2019), thus providing suitable points of comparison. To validate our DNS, we reproduce the results of Tai *et al.* (2011) by using the same Laplace number $J_l = 0.59$, initial thickness $\epsilon = 0.23$, viscosity ratio $m = 0.01$ and density ratio $J_g/J_l = 0.95$. These parameters only slightly differ from the Bian *et al.* (2010) experimental and Romanò *et al.* (2019) numerical studies concerning the Laplace number. These parameters are used only in this § 4.2, while those of table 1 are used in the rest of the paper.

Plateau–Rayleigh instability in a capillary

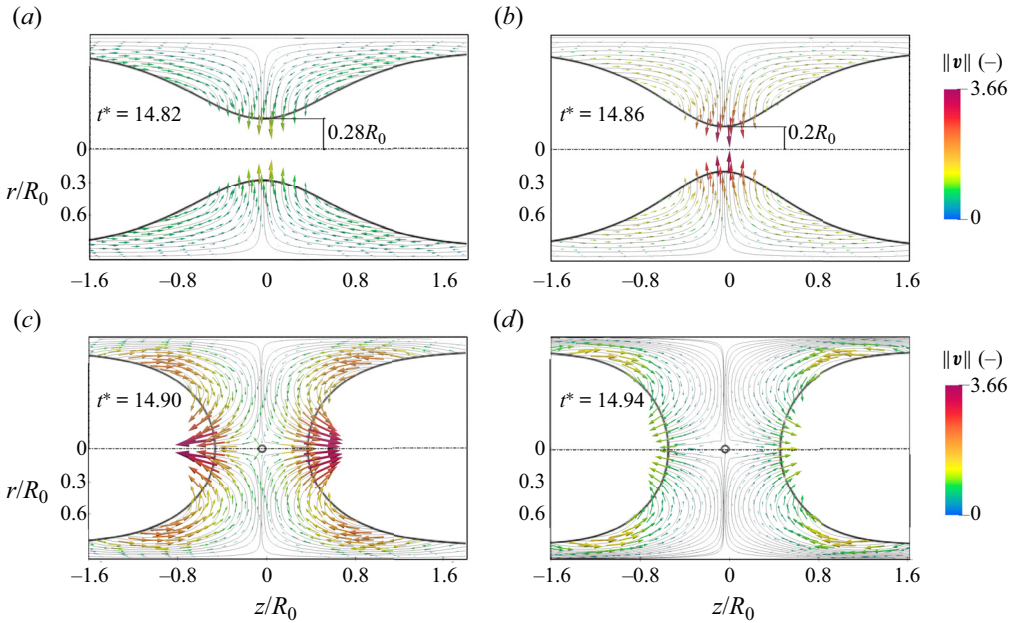


Figure 6. Velocity field around channel occlusion time obtained with DNS. The physical parameters are those of Tai *et al.* (2011). Velocities are scaled by $\sigma \epsilon^3 / \mu_l$ and time by $\mu_l R_0 / \sigma \epsilon^3$ to conform to Tai *et al.* (2011).

The velocity fields are presented in figure 6 just before and just after channel occlusion. Before channel occlusion they qualitatively agree with all aforementioned studies. Liquid is driven from the film dips to the collars where the flow is directed towards the tube centre. A motionless zone is observed at the collar centre, close to the wall. The maximum velocity is encountered at the top of a collar. Few instants before channel occlusion, a strong radial acceleration is observed, the maximum velocity being doubled between the two last pictures. Another zone of local maximum velocity is observed at the transition between the main collar and the thin film, close to the interface. It corresponds to the area where the draining process occurs. After channel occlusion, patterns do not change significantly, although a new pivot in the velocity field is obtained at the centre of the symmetry axis. The liquid pushes the plug axially, increasing its width, which was called bifrontal plug growth by Romanò *et al.* (2019). Velocity is maximal just after channel occlusion. They then decrease until a stationary plug state is reached. In this final state, velocity is maximal in the draining zone joining the plug and the film. All these observations were already made by Tai *et al.* (2011) before channel occlusion and by Bian *et al.* (2010), Romanò *et al.* (2019) after it.

A significant difference is however observed here, as an air bubble is produced in the middle of the plug. Formation of secondary bubbles (or droplets in the case of a liquid jet breakup) has already been observed in other experiments such as those by Tjahjadi, Stone & Ottino (1992). Tjahjadi *et al.* (1992) also explained the process of satellite droplet formation and reproduced their own experimental results with the boundary integral method known for its precision of interface description. Similar bubbles were simulated by Newhouse & Pozrikidis (1992) and Hagedorn, Martys & Douglas (2004). Obtaining a bubble in the middle of a plug is thus normal. One should note that in the Romanò *et al.* (2019) study, VOF simulations were unable to capture small bubbles during collar

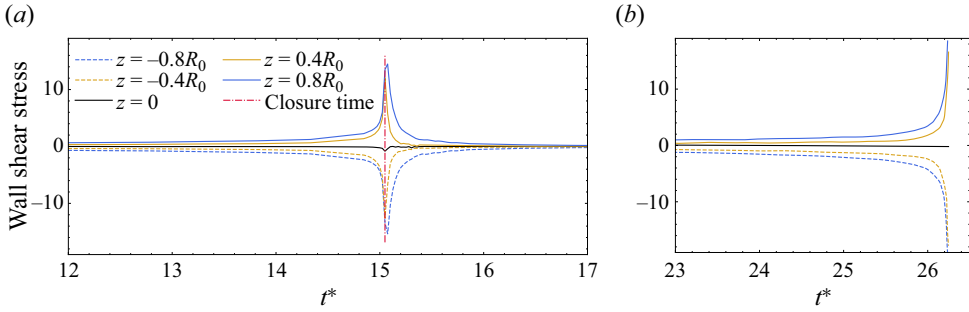


Figure 7. Evolution of the wall shear stress at several locations. Here $z = 0$ corresponds to the approximate location of the maximal film thickness. Time is scaled by $\mu_l R_0 / \sigma \epsilon^3$ and the wall shear stress by $\epsilon^3 \sigma / R_0$ to follow Tai *et al.* (2011). (a) The DNS results from this study; (b) DNS results from Tai *et al.* (2011).

coalescence, probably because of a too large mesh size; Tai *et al.* (2011) could not simulate the plug formation at all.

Velocities are quantitatively in agreement with those of Bian *et al.* (2010), Tai *et al.* (2011), Romanò *et al.* (2019). On the contrary, the channel occlusion time differs considerably. Indeed, as already discussed by Tai *et al.* (2011), it is not a suitable validation metric, as it strongly depends on the initial conditions (amplitude and velocity), which are not the same in different studies.

In the particular field of lungs airway occlusion, on which previous studies focused (Bian *et al.* 2010; Tai *et al.* 2011; Romanò *et al.* 2019), a key parameter is the instantaneous shear stress acting on the channel wall ($\simeq \mu \partial_r v_z$). This parameter is also of significant importance for PEMFC channels, as viscous friction is the main design parameter of channel geometry. The wall shear stress is thus extracted from the previous DNS and plotted in figure 7 at several locations along the tube. Results agree with those of Tai *et al.* (2011). After a slow but steady increase, the shear stress explodes a few moments after channel occlusion. It then reduces even more quickly, as observed by Bian *et al.* (2010). All these results confirm that the DFT numerical method used in this paper can be considered as a reference to investigate the Plateau–Rayleigh instability.

5. Theory

5.1. Governing equations

The previously presented DNS simulations can now be compared with reduced models where inertial and viscous terms can be switched on and off. The present theoretical models use equations and boundary conditions similar to the above numerical approach (cf. § 2). The convective terms $\mathbf{v} \nabla \mathbf{v}$ are however neglected in the Navier–Stokes equations. Thanks to the axial symmetry, the equations and jump conditions reduce to

$$\frac{\partial v_r}{\partial t} = -\frac{1}{\rho} \frac{\partial p}{\partial r} + \nu \left(\frac{\partial^2 v_r}{\partial r^2} + \frac{1}{r} \frac{\partial v_r}{\partial r} - \frac{v_r}{r^2} + \frac{\partial^2 v_r}{\partial z^2} \right), \quad (5.1)$$

$$\frac{\partial v_z}{\partial t} = -\frac{1}{\rho} \frac{\partial p}{\partial z} + \nu \left(\frac{\partial^2 v_z}{\partial r^2} + \frac{1}{r} \frac{\partial v_z}{\partial r} + \frac{\partial^2 v_z}{\partial z^2} \right), \quad (5.2)$$

$$\frac{\partial v_r}{\partial r} + \frac{v_r}{r} + \frac{\partial v_z}{\partial z} = 0, \quad (5.3)$$

Plateau–Rayleigh instability in a capillary

$$[[\mathbf{v}]]_{r=R_i} = 0, \tag{5.4}$$

$$[[\mathbf{n} \cdot \boldsymbol{\Sigma}]]_{r=R_i} = \sigma \kappa \mathbf{n}, \tag{5.5}$$

where $\boldsymbol{\Sigma}$ is the stress tensor and v is the kinematic viscosity. The double brackets denote the interfacial jump. A no-slip boundary condition is taken at the wall in $r = R_0$. Finally, the volume conservation in each phase, in the absence of external flow, results in the relationships

$$2\pi R_i v_i = \frac{\partial Q_l}{\partial z} = -\frac{\partial Q_g}{\partial z}, \tag{5.6}$$

$$Q_l + Q_g = 0, \tag{5.7}$$

where v_i is the interfacial velocity.

5.2. Lubrication model with core fluid

To evaluate the influence of inertia on the development of the Plateau–Rayleigh instability, a model without inertia is first developed to be compared with the DNS. The lubrication theory of Gauglitz & Radke (1988) is extended to consider the core fluid (as it can have significant effects in the plug formation especially when the core radius is small) and a more rigorous account of the cylindrical geometry. The developments are inspired by those of Goyeneche, Lasseux & Bruneau (2002).

The main assumptions for this lubrication model is that the flow is considered laminar and the interface slope is small: $\partial_z h \ll 1$. The interfacial velocity can thus be expressed as

$$v_i \approx -2\pi R_i \frac{\partial h}{\partial t} \approx v_r(R_i). \tag{5.8}$$

The magnitude analysis of the continuity equation results in

$$\frac{v_r}{R_0} \approx \frac{1}{r} \frac{\partial(rv_r)}{\partial r} = -\frac{\partial v_z}{\partial z} \approx \frac{v_z}{\lambda}. \tag{5.9}$$

It is well known that the Plateau–Rayleigh instability does not occur for wavelengths λ smaller than $2\pi R_i$. Hence, the assumption $\lambda \gg R_i \approx R_0$ is valid, leading to $v_z \gg v_r$. A first limit to the lubrication approximation is obtained here, as for $R_i \ll R_0$, smaller wavelengths can become unstable. With a similar magnitude analysis, the velocity derivatives with respect to z can be neglected compared with those with respect to r and (5.1) and (5.2) reduce to

$$\frac{\partial p}{\partial r} = 0, \tag{5.10}$$

$$\frac{\partial p}{\partial z} = \frac{\mu}{r} \frac{\partial}{\partial r} \left(r \frac{\partial v_z}{\partial r} \right). \tag{5.11}$$

Similarly, the jump conditions at the interface become

$$-[[p]] = \sigma \left(\frac{1}{R_i} + \frac{\partial^2 h}{\partial z^2} \right), \tag{5.12}$$

$$\left[\left[\mu \frac{\partial v_z}{\partial r} \right] \right] = 0. \tag{5.13}$$

These equations, coupled to the no-slip boundary condition lead to the thickness evolution equation (cf. Appendix A)

$$-2\pi R_i \frac{\partial h}{\partial t} = \sigma \frac{\partial}{\partial z} \left[\beta \left(\frac{\partial^3 h}{\partial z^3} + \frac{1}{R_i^2} \frac{\partial h}{\partial z} \right) \right], \tag{5.14}$$

where

$$\beta = -\frac{\pi R_i^4}{8\mu_l} \left\{ \frac{(R_0^2 - R_i^2)[4m(R_0^2 - R_i^2) + (3R_i^2 - R_0^2)]}{mR_0^4 + (1 - m)R_i^4} + 4 \ln \left(\frac{R_i}{R_0} \right) \right\}. \tag{5.15}$$

Equation (5.14) is both analysed in the linear regime (§ 6) and numerically solved outside (§ 7). In the linear regime, where the film thickness writes

$$h(z, t) = h_0 + A_0 \exp(i\omega t + ikz), \tag{5.16}$$

(5.14) results in the following dimensionless dispersion relation:

$$\hat{\omega} = x^2(x^2 - 1)\hat{\beta}. \tag{5.17}$$

Here $\hat{\beta} = \beta\mu_l/(2\pi R_i^4)$ and $x = kR_i$ is a dimensionless wavenumber. This number is real, as well as the instability increment (growth rate) $\omega_i = -i\omega$. The dimensionless growth rate is defined as $\hat{\omega} = \omega_i\mu_l R_i/\sigma$.

5.3. Linear stability models accounting for viscosity and inertia

5.3.1. Previous results

As our starting point, we need to mention several previous results. First, Tomotika (1935), following Rayleigh (1878), proposed a general theory considering both viscosity and inertia for both fluids for the case of the fluid jet ($R_0 \rightarrow \infty$). Tomotika investigated the cases where viscosity dominates and where the viscosity ratio is neither zero nor infinite. Tomotika proposed to write the dispersion relation compactly as a matrix \mathbf{M} , the determinant of which is zero. In the present notation, Tomotika’s matrix writes

$$\mathbf{M} = \begin{bmatrix} I_1(x) & I_1(x_g) & K_1(x) & K_1(x_l) \\ xI_0(x) & x_g I_0(x_g) & -xK_0(x) & -x_l K_0(x_l) \\ 2mx^2 I_1(x) & m(x^2 + x_g^2) I_1(x_g) & 2x^2 K_1(x) & (x^2 + x_l^2) K_1(x_l) \\ F_1 & F_2 & 2x^2 K_1'(x) + \hat{\omega} J_l K_0(x) & 2xx_l K_1'(x_l) \end{bmatrix}, \tag{5.18}$$

with

$$F_1 = 2mx^2 I_1'(x) - \hat{\omega} J_g I_0(x) + x \frac{x^2 - 1}{\hat{\omega}} I_0(x), \tag{5.19}$$

$$F_2 = 2mxx_g I_1'(x_g) + x \frac{x^2 - 1}{\hat{\omega}} I_0(x_g). \tag{5.20}$$

Here, I_i and K_i are the i th order modified Bessel functions of the first and second kind, respectively. The prime denotes a derivative. Here x_g and x_l are related to x by

$$x_g^2 = x^2 - \hat{\omega} J_g, \quad x_l^2 = x^2 - \hat{\omega} J_l. \tag{5.21a,b}$$

In parallel to these liquid/gas jet studies, Goren (1962) studied the effect of confinement (finite R_0) by neglecting the core fluid. Goren obtained a 4×4 matrix with different coefficients.

Finally, Georgiou *et al.* (1991) gathered all these models to consider both the core and outer fluids for finite R_0 . Hence, they had to solve the determinant of a 6×6 matrix. However, as their objective was to analyse the impact of electric properties of fluids with similar densities (the outer liquid was an electrolyte and the core, a dielectric fluid) they used a single density and Laplace number for the core and outer fluids.

5.3.2. Present model

In the present study, as the densities of water vapour and liquid water are several orders of magnitude different, the Georgiou *et al.* (1991) model will be generalised for two different fluid densities. We describe here briefly how the dispersion relation is derived and present its final formulation. A more detailed derivation is proposed in [Appendix B](#).

In order to automatically verify the continuity equation (5.3), the radial and axial velocities are expressed with the streamfunction ψ ,

$$v_r = \frac{1}{r} \frac{\partial \psi}{\partial z} \quad \text{and} \quad v_z = -\frac{1}{r} \frac{\partial \psi}{\partial r}. \quad (5.22a,b)$$

Here v_r and v_z are then substituted in the Navier–Stokes equations (5.1) and (5.2) and the pressure terms are eliminated, leading to

$$\left(D - \frac{1}{\nu} \frac{\partial}{\partial t} \right) D\psi = 0, \quad (5.23)$$

where the differential operator $D = \partial^2/\partial r^2 - (1/r)(\partial/\partial r) + \partial^2/\partial z^2$.

It should be noted that in the current linear stability analysis, the convective terms are automatically negligible as they evolve quadratically with the perturbation and are exactly zero for the chosen primary flow.

As D and $(D - \nu^{-1}\partial_t)$ are commutative, when $\nu^{-1} \neq 0$, ψ can be written as a linear combination of ψ_1 and ψ_2 where

$$D\psi_1 = 0 \quad \text{and} \quad \left(D - \frac{1}{\nu} \frac{\partial}{\partial t} \right) \psi_2 = 0. \quad (5.24a,b)$$

Expressing $\psi_j (j = 1, 2)$ as $\psi_j = \phi_j \exp(i\omega t + ikz)$, ϕ_j are solutions of

$$\frac{d^2 \phi_j}{dr^2} - \frac{1}{r} \frac{d\phi_j}{dr} - k_j^2 \phi_j = 0, \quad (5.25)$$

with $k_1 = k$ and $k_2^2 = k^2 + i\omega/\nu$. The solutions of (5.25) are linear combinations of $I_1(k_j r)$ and $K_1(k_j r)$. In each fluid, the streamfunction can then be written as a linear combination of four terms, one for each k_j and for each kind of modified Bessel function (I_1 and K_1). Hence, eight constants are needed to completely define the velocity profile, four in each fluid. This number is reduced to six, as the velocity must be finite in $r = 0$, requiring the K_1 constants in the core fluid to be zero.

The no-slip boundary condition (two equations) and the velocity continuity at the interface (5.4) (two equations) first give four equations. The continuity of the tangential and normal stresses ((5.5) projected to the tangential and normal directions) write in the

small-slope approximation

$$\left[\left[\mu \left(\frac{\partial v_z}{\partial r} + \frac{\partial v_r}{\partial z} \right) \right] \right]_{r=R_i} = 0, \tag{5.26}$$

$$\left[\left[-p + 2\mu \frac{\partial v_r}{\partial r} \right] \right]_{r=R_i} = \sigma \left(\frac{1}{R_i} + \frac{\partial^2 h}{\partial z^2} \right). \tag{5.27}$$

Equation (5.26) leads to the fifth equation. Finally, combining (5.27) with (5.2), (5.6) and (5.7), leads to the last equation

$$\left[\left[-i\omega \frac{\rho}{r} \frac{\partial \psi}{\partial r} + \frac{\mu}{r} \frac{\partial}{\partial r} D\psi + 2ik\mu \frac{\partial v_r}{\partial r} \right] \right] = \frac{k}{\omega} \sigma \frac{(kR_i)^2 - 1}{R_i^2} v_r. \tag{5.28}$$

The set of six equations with six unknowns is homogeneous (Appendix B). Their matrix can be rearranged as

$$\mathbf{M} = \begin{bmatrix} 0 & 0 & K_1(ax) & K_1(ax_l) & I_1(ax) & I_1(ax_l) \\ 0 & 0 & -K_0(ax) & -\frac{x_l}{x} K_0(ax_l) & I_0(ax) & \frac{x_l}{x} I_0(ax_l) \\ I_1(x) & I_1(x_g) & -K_1(x) & -K_1(x_l) & -I_1(x) & -I_1(x_l) \\ I_0(x) & \frac{x_g}{x} I_0(x_g) & K_0(x) & \frac{x_l}{x} K_0(x_l) & -I_0(x) & -\frac{x_l}{x} I_0(x_l) \\ (m-1)I_1(x) & \left[(m-1) - \frac{\hat{\omega} J_g}{2x^2} \right] I_1(x_g) & 0 & \frac{\hat{\omega} J_l}{2x^2} K_1(x_l) & 0 & \frac{\hat{\omega} J_l}{2x^2} I_1(x_l) \\ F'_1 & F'_2 & \hat{\omega} J_l K_0(x) & 0 & -\hat{\omega} J_l I_0(x) & 0 \end{bmatrix}, \tag{5.29}$$

with

$$F'_1 = 2(1-m)x^2 I'_1(x) + \hat{\omega} J_g I_0(x) + x \frac{x^2 - 1}{\hat{\omega}} I_1(x), \tag{5.30}$$

$$F'_2 = 2(1-m)x_g x I'_1(x_g) + x \frac{x^2 - 1}{\hat{\omega}} I_1(x_g). \tag{5.31}$$

Here, $x_{l,g} = k_{l,g} R_i$ are defined by (5.21a,b); $a = R_0/R_i = (1 - \epsilon)^{-1}$ is the radius ratio. We remind that the dispersion relation reads $\det \mathbf{M} = 0$.

In the limit $R_0 \rightarrow \infty$, the first two rows and the last two columns can be dropped from \mathbf{M} so the velocities do not diverge at $r \rightarrow \infty$. The Tomotika (1935) matrix (5.18) is thus found (with some rearrangements). Similarly, if the core gas is forgotten, the first two columns (representing the core fluid) and the third and fourth row (velocity continuity) are dropped leading to the matrix of Goren (1962). Finally, if both fluids have the same densities ($J_l = J_g$), the case of Georgiou *et al.* (1991) without electromagnetic effects is found. Model (5.29) is called the ‘visco-inertial linear model’ hereafter, as it is designed for linear stability studies and accounts for both viscous and inertial terms.

5.3.3. Absence of inertia

In the case where inertia is neglected, $J_l, J_g \rightarrow 0$ and $\det \mathbf{M}$ is trivially zero, as the columns of (5.29) are equal two by two as $x_l = x_g = x$. This comes from the simplification of (5.23) to $D^2 \psi = 0$. To solve this issue, ψ_2 must be modified to be linearly independent of ψ_1 , which is not modified and still verifies $D\psi_1$. Hence, ψ_2 is now a solution of $D\psi_2 = \psi_1$. Therefore, ψ_2 is a linear combination of $r^2 I_0(kr)$ and $r^2 K_0(kr)$. The velocity expressions

detailed in [Appendix B](#) are modified accordingly. Using the same boundary conditions, the matrix \mathbf{M} is modified and rearranged as

$$\mathbf{M} = \begin{bmatrix} 0 & 0 & K_1(ax) & axK_0(ax) & I_1(ax) & axI_0(ax) \\ 0 & 0 & -K_0(ax) & f_k(ax) & I_0(ax) & f_i(ax) \\ I_1(x) & xI_0(x) & -K_1(x) & -xK_0(x) & -I_1(x) & -xI_0(x) \\ I_0(x) & f_i(x) & K_0(x) & -f_k(x) & -I_0(x) & -f_i(x) \\ (m-1)I_1(x) & mI_1(x) + (m-1) \\ & \times xI_0(x) & 0 & K_1(x) & 0 & -I_1(x) \\ G'_1 & G'_2 & K_1(x) & 0 & I_1(x) & 0 \end{bmatrix}, \tag{5.32}$$

with

$$f_k(x) = 2K_0(x) - xK_1(x), \tag{5.33}$$

$$f_i(x) = 2I_0(x) + xI_1(x), \tag{5.34}$$

$$G'_1 = (1 - m)xI_0(x) + (m - 2)I_1(x) + \frac{x^2 - 1}{2\hat{\omega}}I_1(x), \tag{5.35}$$

$$G'_2 = (1 - m)x^2I_1(x) + x\frac{x^2 - 1}{2\hat{\omega}}I_0(x). \tag{5.36}$$

As in Tomotika (1935), this matrix can also be obtained by letting $J_l, J_g \rightarrow 0$ in (5.29). Unlike the lubrication theory, our model does not assume the axial and radial velocities to be independent. All terms of the viscous contribution to the Navier–Stokes equations (5.1) and (5.2) are considered. Model (5.32) is subsequently referred to as the ‘viscosity-only linear model’.

5.3.4. Absence of viscosity

In the absence of viscosity, the Navier–Stokes equations reduce to those of Euler. Hence, ψ now verifies $D\psi = 0$, leading to $\psi = \psi_1$ only. Hence, the second, fourth and sixth columns in (5.29) disappear. Moreover, the absence of viscosity removes the tangential no-slip wall condition and the tangential stress and velocity continuity conditions at the interface. The second, fourth and fifth rows disappear and (5.29) simplifies to

$$\mathbf{M} = \begin{bmatrix} 0 & K_1(ax) & I_1(ax) \\ I_1(x) & -K_1(x) & -I_1(x) \\ F'_1 & \hat{\omega}J_lK_0(x) & -\hat{\omega}J_lI_0(x) \end{bmatrix}, \tag{5.37}$$

with $F'_1 = x((x^2 - 1)/\hat{\omega})I_1(x) + \hat{\omega}J_gI_0(x)$. Note that, although μ_l is present in the scaling of both $J_{l,g}$ and $\hat{\omega}$, it cancels out of the dispersion relation. Model (5.37) is subsequently referred to as the ‘inertia-only linear model’.

6. Growth rate analysis

Having at hand all the previously developed models, it is now possible to evaluate the relative contribution of the different effects. The dispersion relation $\det(\mathbf{M}) = 0$ is solved with the SymPy library of Python.

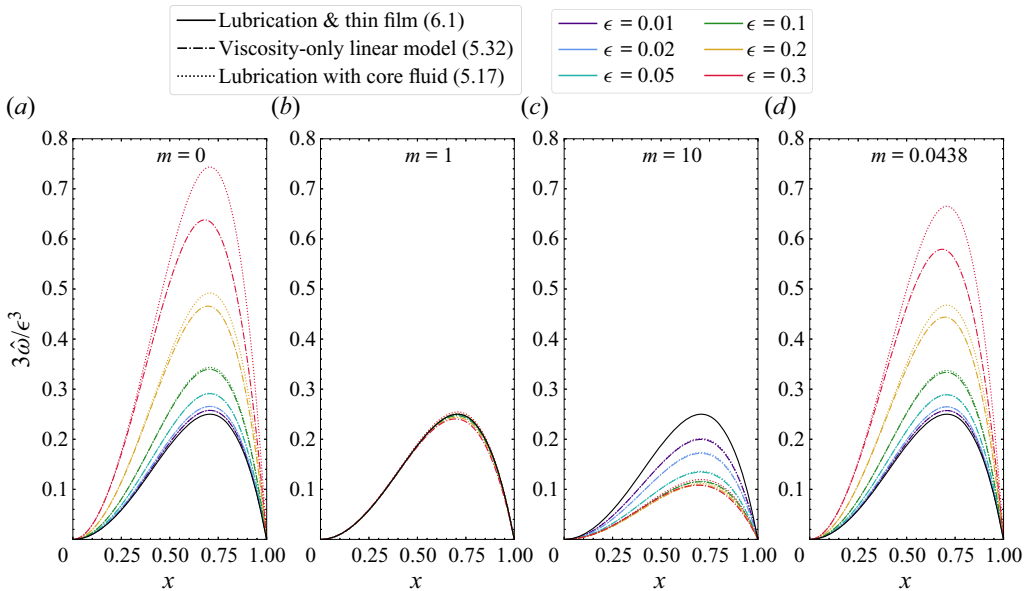


Figure 8. Impact of the viscosity ratio m on the convergence of the growth rate to the thin film approximation. Different colours indicate the average film thickness ϵ . Results are shown for (a) $m = 0$, inviscid core fluid; (b) $m = 1$, equal viscosities of core and outer fluids; (c) $m = 10$, more viscous core fluid; (d) $m = 0.0438$ corresponding to the water parameters of table 1. Solid lines: thin film lubrication model (6.1). Dash-dotted lines: viscosity-only model (5.32). Dotted lines: lubrication model (5.17).

6.1. Influence of the core fluid

While most thin film models in microscopic tubes consider only the outer fluid (Goren 1962; Hammond 1983; Frenkel *et al.* 1987; Gauglitz & Radke 1988; Johnson *et al.* 1991; Eggers & Dupont 1994; Lister *et al.* 2006a), some authors include the effect of the core, which substantially complicates the theory (Georgiou *et al.* 1991; Halpern & Grotberg 2003; Dietze & Ruyer-Quil 2015; Camassa *et al.* 2017). Nevertheless, a quantitative evaluation of the core flow effect appears relevant when analysing plug formation, especially to later investigate the conditions under which the Plateau–Rayleigh instability can be saturated by an imposed core gas flow. In this section we thus analyse the influence of the core fluid on the linear stability in two steps. First the analysis will be restricted to the viscous problem modelled by the viscosity-only linear model (5.32) and by the lubrication dispersion relationship (5.17). Then a similar analysis will be performed on the inertial problem modelled by the inertia-only linear model (5.37).

Figure 8 presents the results of several simulations for various values of m and h_0 and for both the lubrication with the core fluid model and the viscous linear one. In order to obtain similar orders of magnitude for different ϵ , and thus, to better observe the differences due to the viscosity ratio, the growth rates are scaled by $\epsilon^3/3$. Indeed, in the thin film limit, a Taylor expansion of (5.17) at leading order in terms of the dimensionless film thickness $\epsilon = h_0/R_0$ results in

$$\hat{\omega} = \frac{\epsilon^3}{3}(x^2 - x^4). \tag{6.1}$$

Figure 8 shows that, whatever the viscosity ratio is, the curves converge towards the classical thin film lubrication approximation (6.1) (plotted with a solid line) when $\epsilon \rightarrow 0$.

However, this convergence is much quicker for the particular case of fluids with equal viscosities (figure 8*b*). Indeed, the Taylor expansion of (5.17) can be pursued at the next order with respect to ϵ giving

$$\hat{\omega} = \frac{\epsilon^3}{3}(1 + 3(1 - m)\epsilon)(x^2 - x^4). \quad (6.2)$$

The second-order term disappears for $m = 1$. This explains the observation of Georgiou *et al.* (1991) that the agreement between their model and the classical lubrication (6.1) is ‘exceptional even for ϵ as large as 0.2’. Moreover, in the other cases, (6.2) proves that the instability is accelerated for thicker films if $m < 1$ (the core fluid is less viscous than the outer one; see first and last plots). On the contrary, if the core fluid is more viscous (figure 8*c*), the instability slows down for thick films.

Such observations stress the importance of the core fluid effect. Indeed, compared with the case without core fluid (figure 8*a*), the growth rate is reduced in the practically important water case (figure 8*d*). The core gas slightly slows down the instability in thick films.

Finally, the lubrication model with core fluid (5.17) appears to agree with the viscosity-only linear model (5.32) where all viscous contributions to the Navier–Stokes equations are considered. The agreement is perfect for thin films or highly viscous core fluids but is still reasonable for thicker films and less viscous core fluids. This validates the use of the lubrication with the core fluid model (5.14) to predict the nonlinear evolution of the system in the absence of inertia (see § 7.2).

Concerning the inertial contribution of the core fluid, it is *a priori* expected to be negligible as the Laplace number J_g of the core fluid is two orders of magnitude smaller than that of the liquid film J_l . However, the effect of the density ratio for other fluids can be studied. When considering the inertia-only problem (5.37), the lubrication reference curve becomes irrelevant and must be modified by the thin film limit

$$\hat{\omega} = x\sqrt{1 - x^2} \frac{\sqrt{\epsilon}}{\sqrt{J_l}} \quad (6.3)$$

of the inertia-only model (5.37). Figure 9 provides the dispersion curves that come from (5.37) for several density ratios J_g/J_l . The reference curve in black is (6.3). To obtain results with similar magnitudes, the growth rates are scaled by $\sqrt{\epsilon/J_l}$.

Similarly to the above viscosity-only analysis, growth rates for the inertia-only model (5.37) tend towards the thin film limit (6.3) when $\epsilon \rightarrow 0$ whatever the density ratio is. Moreover, an increase in the core fluid density results in a decreasing growth rate, meaning the Plateau–Rayleigh instability slows down. Indeed, the denser the core fluid, the more difficult it is to displace. The fastest convergence to the thin film approximation is found for an intermediate density ratio $J_g/J_l = 3/4$ (this can be obtained by pursuing the Taylor expansion of (5.37) at the next order in ϵ). Finally, as in the above viscosity-only case, no clear difference between the real case scenario of figure 9(*d*) and the coreless scenario of figure 9(*a*) can be noticed. As expected, the inertial contribution of the core gas can thus be safely neglected.

6.2. Transition between viscous and inertial regimes

We now consider the practical case of water (table 1) that corresponds to $m = 4.38 \times 10^{-2}$, $J_l = 3.6 \times 10^5(1 - \epsilon)$ and $J_g = 224.3(1 - \epsilon)$. With these parameters, the viscosity-only, inertia-only and visco-inertial linear stability models (5.32), (5.37) and

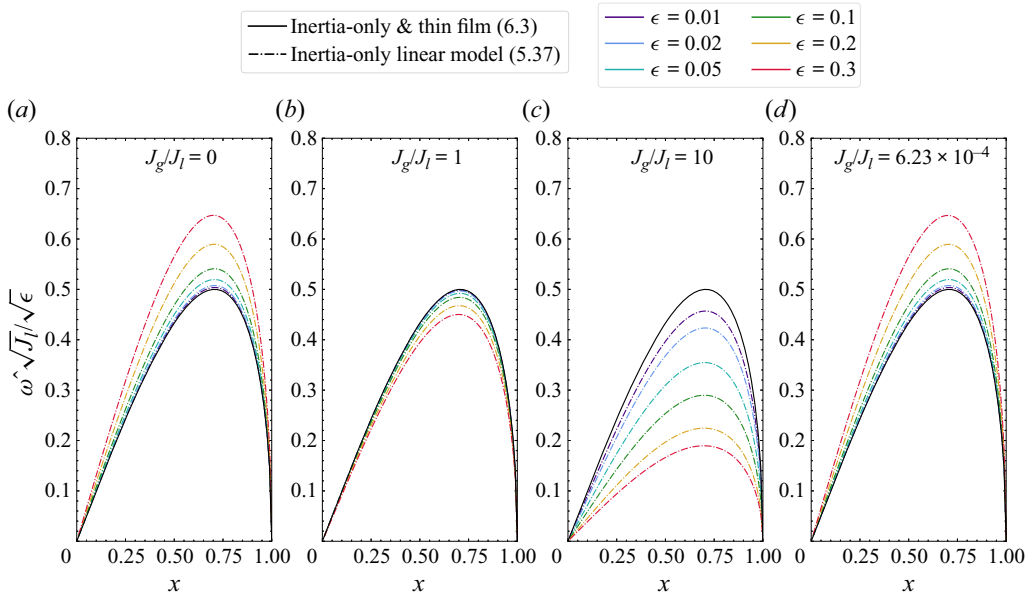


Figure 9. Impact of the density ratio J_g/J_l on the growth rate. Different colours indicate the average film thickness ϵ . Results are shown for (a) $J_g = 0$, no core fluid; (b) $J_g = J_l$, equal densities of core and outer fluids; (c) $J_g = 10J_l$, denser core fluid; (d) $J_g = 6.23 \times 10^{-4}J_l$ corresponding to the water parameters of table 1. Solid lines: inertia-only thin film model (6.3). Dash-dotted lines: inertia-only linear model (5.37).

(5.29) are solved and compared in figure 10 for different ϵ values. As in figure 8, growth rates are scaled by $\epsilon^3/3$.

Direct numerical simulations are also performed for different initial perturbation wavelengths to find the growth rates in the linear regime. Their determination is discussed in Appendix C. The obtained growth rate is plotted as a function of the wavenumber with triangle characters in figure 10. Due to the incoherence of initial conditions in DNS and in the theory (cf. Appendix C), the exponential growth stage does not start at $t = 0$ and should thus be identified. This causes uncertainties illustrated with error bars. During this process, it is particularly important to ensure that the measured growth rate is associated to the correct wavelength. Indeed, the final wavelength of the perturbation can be different from the initial one as it is always shifted towards that of the maximal growth rate. Direct numerical simulations include all the relevant phenomena: viscosity, capillarity, convection and inertia.

The viscosity-only model (5.32) agrees with DNS for thin films ($\epsilon \leq 0.1$), cf. figure 10(a). Small discrepancies appear only close to the maximum growth rate. However, significant differences occur for thicker films. While the viscosity-only model results in a positive deviation from the thin film lubrication approximation, the growth rate of the instability is actually lower.

On the contrary, the inertia-only model (5.37) agrees with DNS for thick films $\epsilon \geq 0.3$ (cf. figure 10b) while the model strongly differs at small ϵ . This clearly indicates a transition from a viscous regime for $\epsilon \leq 0.1$ to an inertial regime for $\epsilon \geq 0.3$. In the overall picture, both terms are essential to capture the instability inception. This is apparent in figure 10(c) where DNS is compared with the visco-inertial linear model (5.29). Here, the agreement is of high quality whatever the average film thickness.

Plateau-Rayleigh instability in a capillary

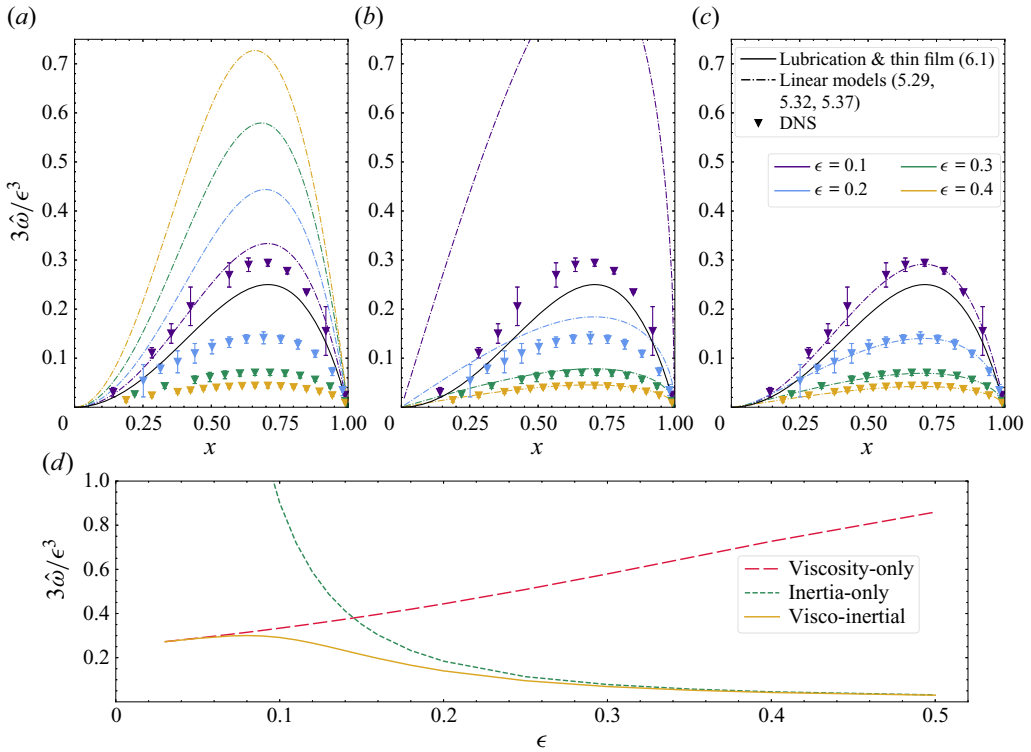


Figure 10. Comparison of the effects of inertia and viscosity on the growth rate. (a–c) Dispersion curves for the three linear stability models: (a) viscosity-only model, (b) inertia-only model, (c) visco-inertial model. Different colours indicate the average film thickness ϵ . Dash-dotted lines: linear stability model. Solid lines on all graphs: thin film lubrication approximation (6.1). Triangle characters on all graphs: growth rates extracted from DNS. (d) Maximum growth rate as a function of ϵ . All curves are from linear stability models, either viscosity-only (long red dashes), inertia-only (green dashes) or visco-inertial (yellow solid line).

Since the visco-inertial linear model agrees with DNS, it can be used to obtain the maximum growth rate for several thicknesses. The results are plotted in figure 10(d) and are compared with the inertia-only and viscosity-only linear models. The cross-over between these regimes is clear here: while for $\epsilon \lesssim 0.1$, the maximum growth rate follows the viscosity-only curve, it corresponds to the inertia-only model for $\epsilon \gtrsim 0.25$. In the transition zone $0.1 \leq \epsilon \leq 0.25$, both viscosity and inertia are important.

The inertial regime validity for thick films shows that the core vapour can be neglected in the water vapour/liquid water system. Indeed, with the physical parameters of table 1, the core gas effect was observed only for thick films in the viscosity-only model of figure 8. However, as demonstrated above, these films actually follow the inertial regime where the core gas does not affect the growth rates (figure 9). Hence, the core gas has almost no influence on the linear regime of the Plateau-Rayleigh instability. Such a conclusion can be verified with the visco-inertial linear model, within which the curves with or without the core gas perfectly overlap (this was verified by the authors).

Finally, a significant outcome of figure 10(b) is that, for the chosen physical system, the prediction of the inertial linear model is higher than that of the thin film lubrication for thin films and lower for thick films. Indeed, in the absence of viscosity, the growth rate vanishes for $\epsilon \rightarrow 1$ while it takes a finite value in the thin film approximation, meaning

that the ratio diverges accounting for the ϵ^3 lubrication scaling. The ϵ^3 scaling is replaced in that case by the $\sqrt{\epsilon}$ scaling of (6.3).

In the present paper a no-slip condition has been imposed at the wall. This choice is reasonable for the millimetric film-covered channels studied here, although at small scale this condition can break down. Zhao, Zhang & Si (2023) studied the effects of slip on the linear stability of Plateau–Rayleigh instability and demonstrated that it speeds up its development, notably for thin films and micrometric channels. This enhancement of the instability equally affects the nonlinear regime, for example, by accelerating the film thinning (Liao, Li & Wei 2013), which may modify the critical thickness separating stable collars and plugs due to volume retention in satellite lobes as discussed later in §§ 7.2 and 7.3. Slip is finally expected to increase the wavelength of maximum instability (Zhao *et al.* 2023).

In this section a transition between an inertial and a viscous regime has been discussed for small perturbations. In the next section the underlying mechanisms of this transition will be studied by enlarging the previous temporal study to observe spatial dependencies of viscous and inertial contributions, both in the linear and nonlinear regimes.

7. Distribution analysis of Navier–Stokes terms and their effects

Direct numerical simulations offer the opportunity to access the evolution and spatial distribution of any variable. In particular, it is possible to obtain the relative contributions to the pressure gradient of the inertia $\rho \partial_t \mathbf{v}$, viscosity $\mu \nabla(\nabla \mathbf{v})$ and convection $\rho \mathbf{v} \cdot \nabla \mathbf{v}$ terms of the Navier–Stokes equations. Except at the interface where capillary forces are of course essential, these terms completely define the dynamics. By plotting these contributions in the outer fluid, we are able to confirm the previous conclusions on the linear regime and to extend them to the nonlinear evolution of plugs and collars.

7.1. Comparative analysis of forces in the linear regime

We first confirm and refine the previous linear regime results. Figure 11 presents a map of the magnitudes of the three aforementioned contributions in the linear regime of DNS, for a mostly viscous case ($\epsilon = 0.1$) and a transitional visco-inertial case ($\epsilon = 0.2$). The colour scales differ between figures to show the spatial variation of each term. The simulation times have been chosen arbitrarily within the regime of exponential growth. Results have been checked at twice these times and give very similar results with slightly higher magnitudes.

First, one can confirm that convection can be neglected in the above linear models. Its contribution is at least one order of magnitude smaller than those of inertia and viscosity. Moreover, all contributions are negligible in the core flow, thus supporting results from § 6. In the thin film case $\epsilon = 0.1$, as expected, the viscous contribution largely dominates that of inertia, being one order of magnitude higher. When $\epsilon = 0.2$, inertia and viscosity terms are comparable in agreement with the previous discussion. Inertia is slightly more important, being present within a larger domain of the liquid.

A clear spatial separation between inertia and viscosity is also observed, the former acting mostly near the interface while the latter is maximal close to the wall. Such a separation is present at any time in all simulations, in both linear and nonlinear regimes. From an energy point of view, the energy can only come from surface tension forces acting at the interface. This energy is converted into kinetic energy, then transported to the wall and finally dissipated there by viscosity. In the thin film case, the main kinetic transport contribution seems to be the viscous diffusion, which does not depend on r

Plateau–Rayleigh instability in a capillary

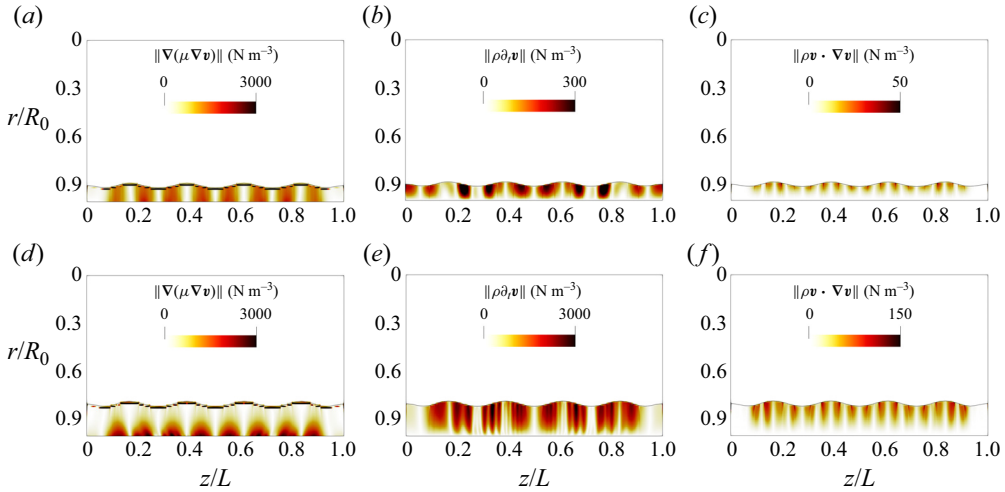


Figure 11. Spatial dependence of the contribution of viscosity (*a,d*), inertia (*b,e*) and convection (*c,f*) in the linear regime obtained by DNS. Data for $\epsilon = 0.1$ at $t = 10$ ms are shown in (*a–c*), while those for $\epsilon = 0.2$ at $t = 5$ ms are presented in (*d–f*). Note the different colour scale for different subfigures.

and is everywhere higher than inertia. In the thick film case, however, kinetic energy is transported mostly by inertial forces; the viscous diffusion is much smaller at the interface. In practice, the transition between the viscous and the inertial regime is a transition between a diffusive and a direct inertial transport process of kinetic energy. The inertia, viscous and convection terms are maximal at the collar edges and minimal inside them. The dynamics is thus mostly driven by what happens at the collar edges.

7.2. Nonlinear formation of satellite lobes

Extensive studies of the long-term behaviour of thin films were previously carried out, notably by Hammond (1983) and Lister *et al.* (2006*a*). Based on a simple lubrication model, Hammond (1983) studied the formation and evolution of satellite lobes that appear between the main collars. Hammond (1983) simulations were restricted to domains where main collars cannot move. Lister *et al.* (2006*a*) extended this study and discovered that main collars and satellite lobes can exhibit a sliding motion. In both studies, only viscous lubrication models were used, which underlines the crucial role of viscosity in long-term thin film dynamics. Satellite lobe formation is explained by the interplay of several effects. Initially, the film dips as they have a larger interface radius present a higher capillary pressure. Liquid is thus drained from dips to collars, which is the primary instability mechanism. It is only valid for long wavelengths where the axial curvature $\partial_{zz}h$ is smaller than the radial one. However, as the film thins, viscous forces become significant, slowing down the drainage process. Viscous forces, at first order, are proportional to h^{-3} . Hence, they are bigger at the dip centre than on the main collar edges. As a consequence, the dip flattens. In a flat film portion the pressure gradients vanish, thus stopping the drainage. However, the flow persists close to collars where the film slope is non-zero. This creates new local minima and satellite lobes. These lobes have a smaller axial extent and are stable against the Plateau–Rayleigh mechanism as their axial curvature dominates their radial one, explaining why they are finally drained into the main collars. A similar mechanism is also observed in the Rayleigh–Taylor instability (Lister, Rallison & Rees 2006*b*), which is well described in Dietze, Picardo & Narayanan (2018, figure 2).

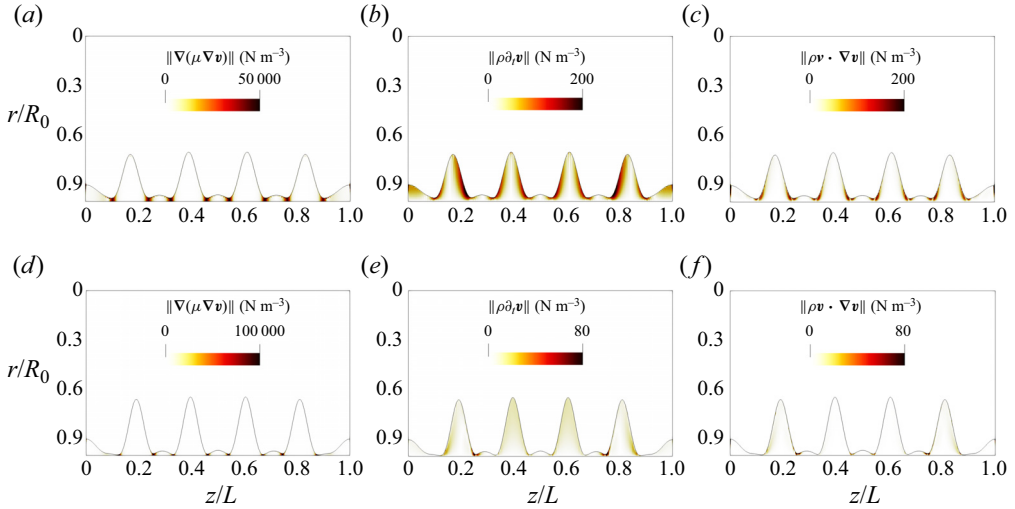


Figure 12. Spatial dependence of the contribution of viscosity (a,d), inertia (b,e) and convection (c,f) at satellite lobe formation obtained by DNS. Data for $\epsilon = 0.1$ at $t = 100$ ms are shown in (a–c), while those at $t = 300$ ms are presented in (d–f). Note the different colour scale for different subfigures.

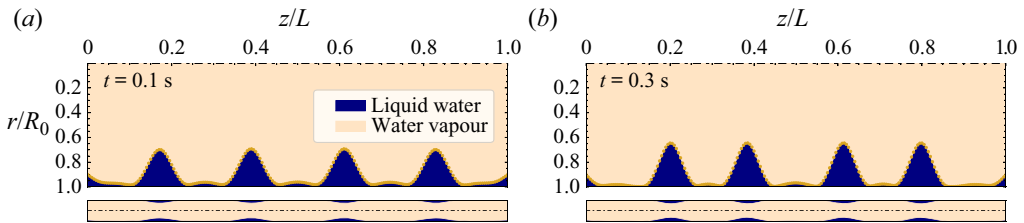


Figure 13. Interface shapes obtained with lubrication equation (5.14) for the same parameters as figure 12.

These lobes are observed in our DNS, cf. figure 4(b) (slightly visible e.g. at $z = 0.35L$) and figure 12. They can be equally obtained by solving numerically the lubrication equation (5.14). Figure 13(a) illustrates one time step soon after the satellite lobes formation obtained with (5.14). The ability of the lubrication approximation to recover DNS results confirms that satellite lobe formation is only driven by viscous and capillary forces but not by inertia. This result was already present in the fact that Lister *et al.* (2006a); Dietze *et al.* (2018) found similar results, although the latter model included the inertial and convective terms while the former considered only the viscosity contribution. Figure 12(a–c) demonstrates that viscous terms are several orders of magnitude larger than those of inertia and convection during the satellite lobe development. We note that the viscous forces on the wall evolve nearly linearly with time, while both inertia and convection diminish over time; the film evolution becomes quasi-static.

At large time scales, as expected by Lister *et al.* (2006a), Dietze & Ruyer-Quil (2015), Dietze *et al.* (2018), collars start sliding. We observe such an effect both in DNS and lubrication results, although not identically. In DNS the collars direct themselves to the domain centre, while within the lubrication approach (figure 13b), they get closer two by two. One probable explanation for this is that lateral boundary conditions are not exactly identical in DNS and lubrication simulations. Finally, lobes and collars can collide and either merge (thus creating bigger collars or even plugs) or rebound without merging, as

expected by Lister *et al.* (2006a). It is not possible to know which of these two scenarios will occur as DNS results become uncertain when the film thins too much. Indeed, DNS results should be assumed valid only when at least 10 mesh cells are present in the film. An adaptive mesh would solve this problem but is not yet implemented. Overall, even during the sliding motion, inertial and convective contributions are negligible compared with viscous forces, as observed in figure 12 just before ($t = 100$ ms) and during ($t = 300$ ms) sliding.

7.3. Nonlinear plug formation

In this section we examine the nonlinear channel occlusion phenomenon that occurs for thick films.

7.3.1. Plug formation time

As the lubrication equation has proven to be invalid in the linear regime, it cannot be used for this case. We first consider the occlusion times for a given ϵ . Assuming the linear regime during all the evolution (which is, of course, untrue), the occlusion time is expected to be defined by the growth rate ω_i as

$$t_{plug}^{lin} = \ln \left[\frac{(1 - \epsilon)R_0}{A_0} \right] \frac{1}{\omega_i}, \quad (7.1)$$

where A_0 is the amplitude of the initial perturbation and $(1 - \epsilon)R_0 = R_i$ is the initial core vapour radius. It corresponds to the radius to fill to close the channel. Figure 14 compares the value of (7.1) and t_{plug} observed in DNS. For thick films ($\epsilon \geq 0.14$), $t_{plug}^{lin} \propto t_{plug}$ and the occlusion time is regularly overestimated by (7.1). It indicates that the behaviour in the nonlinear regime is probably similar to the linear regime, but that it is accelerated close to the tube centre. However, this observation does not stand for films of thickness just above ϵ_{cr} , where the occlusion is strongly delayed ($t_{plug} \gg t_{plug}^{lin}$) as already observed in figure 5. Dietze & Ruyer-Quil (2015) have explained this delay by a ‘viscous-blocking’ mechanism where the viscous dissipation slows down the instability and allows the formation of satellite lobes between primary collars (which is discussed in the previous section for thin films). The liquid volume available for plugs is thus reduced and occlusion is not observed. It may explain the discrepancy between the critical volume obtained on the one hand by Gauglitz & Radke (1988) and by us, cf. § 4.1 and on the other hand by Everett & Haynes (1972).

Figure 15 evaluates the different contributions to the pressure gradient for the case $\epsilon = 0.2$ at three stages: well before the channel occlusion, immediately before and after. Long before channel occlusion, as in the linear regime, viscous and inertial forces have similar orders of magnitude while being spatially separated. Nevertheless, convection becomes significant, though still smaller than other contributions. As expected, this regime is similar to the linear regime.

Just before the channel occlusion, a strong increase of inertial and convective contributions is observed at the top of the rising collar. This increase agrees with Gauglitz & Radke (1988) who mentioned that a clear acceleration in the rising process is observed when the film reaches a thickness of $0.6R_0$, cf. figure 5. Such high values of inertia and convection in the tip of the collar is due to the cylindrical geometry: as the collar rises, it has a smaller space to fill, while still accelerating due to the exponential behaviour of the Plateau–Rayleigh instability. This phenomenon appears very briefly (here during approximately $1 \mu\text{m}$), explaining why t_{plug}^{lin} approximates well t_{plug} .

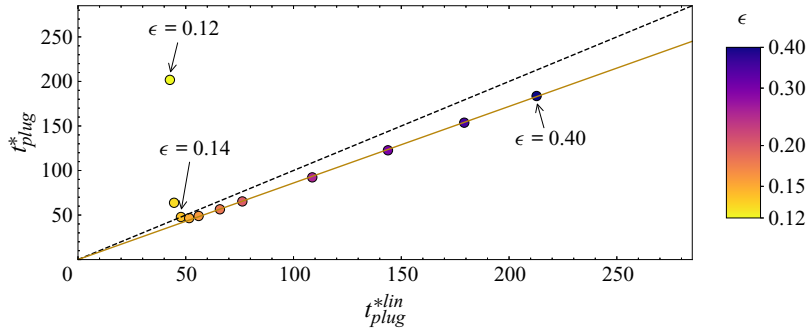


Figure 14. Dimensionless occlusion time observed in DNS compared with the dimensionless occlusion time predicted from the linear regime via (7.1). Time is scaled by $\mu_l R_0 / \sigma \epsilon^3$. The solid orange line is a linear fit to the points with $\epsilon > 0.15$. Its slope is 0.86 with a regression coefficient 0.99989. The dashed black line is $t_{plug}^{*} = t_{plug}^{*lin}$.

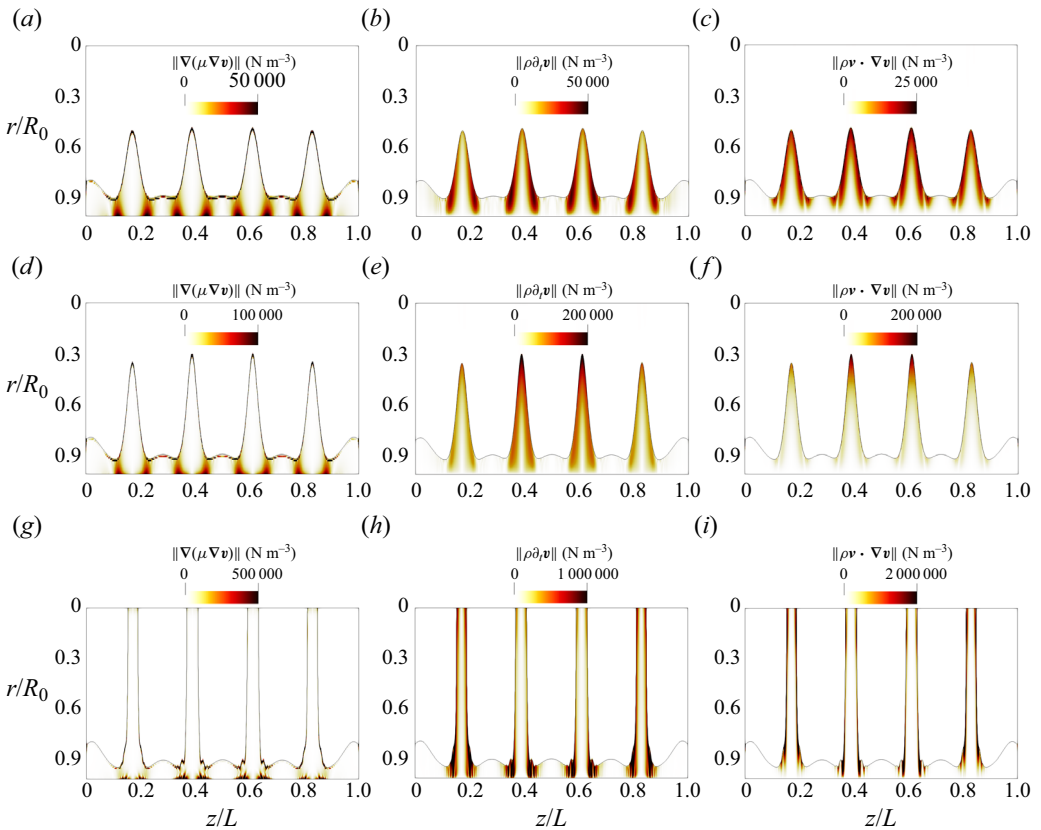


Figure 15. Spatial dependence of the contribution of viscosity (a,d), inertia (b,e) and convection (c,f) in the linear regime obtained by DNS. Data for $\epsilon = 0.2$ at $t = 18$ ms are shown in (a–c), those at $t = 19$ ms are in (d–f) and those at $t = 20$ ms are presented in (g–i). Note the different colour scale for different subfigures.

Such a concentration of inertia and convection at the tip of the rising collar seems to point towards a transition between a regime where inertia/convection and viscous forces are both significant but spatially separated and a regime where the collar growth is only

Plateau–Rayleigh instability in a capillary

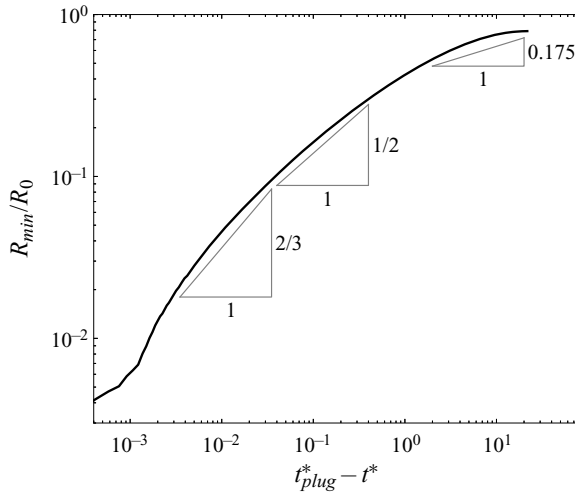


Figure 16. Log-log plot of the core gas throat radius R_{min} against $t_{plug}^* - t^*$, the time remaining before occlusion. The case is for $\epsilon = 0.2$. Times are scaled by $\mu_l R_0 / \sigma \epsilon^3$.

governed by inertial and convective contributions. To confirm this analysis, the evolution of the core gas throat radius $R_{min} = R_0 - h_{max}$ is plotted against the time remaining before plug formation $t_{plug} - t$ in figure 16. A log-log scale is used to identify the relevant power laws. For the breakup of liquid jets, Eggers & Villermaux (2008) identified three scaling laws $R_{min} \propto (t_{plug} - t)^\alpha$. First, when inertia and surface tension effects are balanced, the dimensional analysis predicts $\alpha = 2/3$. If viscous terms and surface tension are balanced, $\alpha \approx 0.175$. Finally, in the case where all three contributions are important, $\alpha = 1/2$. Although these laws were derived for the case where only the inner fluid is considered, it is reasonable to assume that they are still relevant for the outer fluid case. However, one mentions that the inner fluid should play a significant role when R_{min} becomes sufficiently small. As R_{min} decreases, it appears to follow a time scaling with increasing exponent (figure 16) without scale separation. The slope mostly varies between 1/2 once the regime is well established and 2/3 close to the channel occlusion. This suggests a continuous transition from a regime where the viscous contribution is significant to a regime where it becomes insignificant compared with inertia in the late stage of occlusion. The slope 0.175 is not clearly discernable at the beginning. Such results can be compared with those of Tai *et al.* (2011) with more viscous fluids. In their case, the slopes 0.175 and 1/2 were both clearly identified, highlighting the relevance of viscosity all along the occlusion process and of inertia only in its late stages. Finally, the collar tip flattens just before plug formation (see figure 18b), which can be caused by the resistance of the inner fluid.

7.3.2. Capillary waves

The plug formation by coalescence generates capillary waves that propagate along the plug edges towards the thin film. Those are driven by inertia and convection, as observed in figure 15(g,h). They then rebound several times on the plug feet and are gradually dissipated by viscous forces at the channel wall. The rebounds appear because the viscous forces are smaller than inertial contributions, requiring time to dissipate capillary waves. These capillary waves can notably be important for the pressure drop and wall shear stress evaluation, as illustrated by figure 17, which presents the evolution of the wall shear

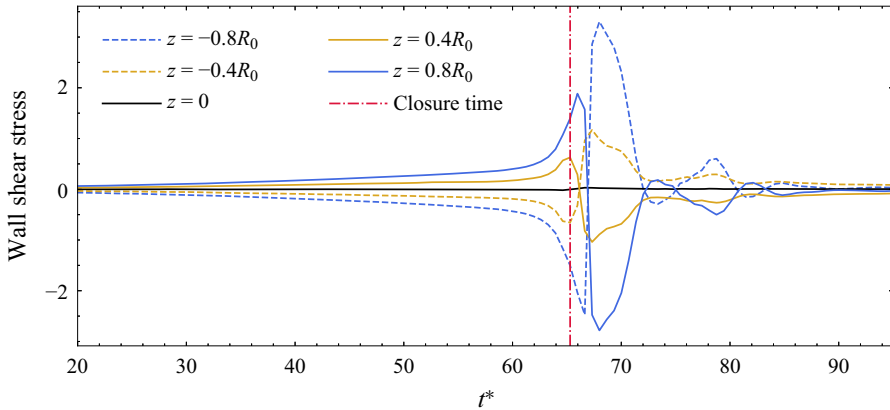


Figure 17. Evolution of the wall shear stress at several locations. Here $z = 0$ corresponds to the approximate location of the maximal film thickness. Time is scaled by $\mu_l R_0 / \sigma \epsilon^3$ and the wall shear stress by $\epsilon^3 \sigma / R_0$, as in Tai *et al.* (2011).

stress around a plug. Unlike figure 7 where the Laplace number of the film is smaller (meaning that the viscous effects are more important compared with inertia), the main peak occurring just after channel occlusion is followed by several significant aftershocks.

A better understanding of these capillary waves can be obtained with the spatio-temporal diagram of the film thickness presented in figure 18(a). The outer liquid thickness h/R_0 is represented with the colour scale. Only the domain between the two central plugs is plotted. Plugs are shown in red and holes in dark blue. Several interface profiles at times and locations indicated by the black vertical lines in figure 18(a) are also provided in figure 18(b–g). Initially, the collars are rising around $z = 0.39L$ and $z = 0.61L$ while the dip between the collars evolves into a satellite lobe surrounded by two holes (initially at $\approx 0.45L$ and $0.55L$). Around $t^* = 65$, the collar quickly accelerates to form plugs. The moment of plug formation corresponds to the first red line in figure 18(a). After that and for quite a short time, the plug thickness near the tube axis becomes slightly larger than closer to the wall (figure 18c), which corresponds to the co-existence of two plug heights in figure 18(a) and a bulge of the red zone. Therefore, a lighter red zone confined between the first red line and the rest of the plug is observed. Such an hourglass shape of the plug interface is due to the liquid accumulation near the tube axis just after coalescence. Indeed, the concentration of inertia and convection at the top of the collar observed in figure 15(e,f) has reached the tube axis and cannot go further. Hence, liquid accumulates at the tube axis, quickly widening there. This generates an inertial capillary wave that propagates from the axis towards the wall, along the plug edges (figure 18d). When it reaches the plug foot, it strongly thins the film there, separating the flow in the plug and in the satellite lobe. This, in turn, perturbs the satellite lobe and generates several capillary waves close to the plug foot, with different wavelengths and velocities. The larger wave is the closest to the plug foot and is also the slowest one, as observed in the spatio-temporal diagram. Capillary waves then propagate along the satellite lobe interface, interact with each other, and are eventually dissipated by viscous forces at the plug foot (figure 18e,g). Due to the strong film thinning at the plug foot, they never re-enter the plug, as observed in figure 15(g). Notably, while the interaction of capillary waves does not seem to attenuate them, they are strongly damped after an interaction with the plug foot (figure 18a). Note that during this whole process the plug edges remain almost motionless as shown by the horizontal red zone edges in figure 18(a).

Plateau–Rayleigh instability in a capillary

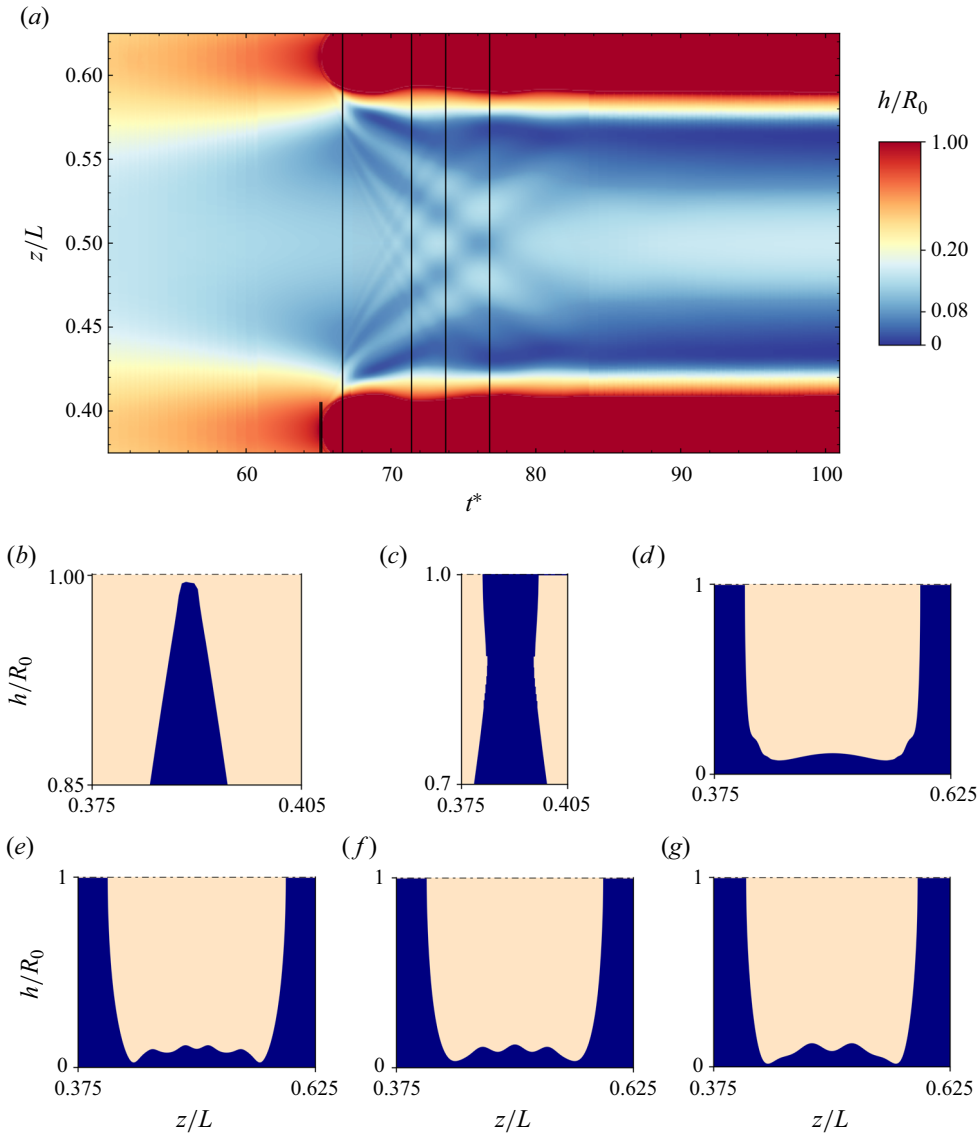


Figure 18. (a) Spatio-temporal diagram of the simulation for $\epsilon = 0.2$ around plug formation, in the central part of the domain. Plugs are represented in red and holes in dark blue. Time is scaled by $\mu_l R_0 / \sigma \epsilon^3$ and length by L . (b–g) Phase distributions at six different times and for different spatial domains, represented by the six vertical lines in (a). Liquid water is represented in blue and water vapour in beige, as in figure 4. Results are shown for (b) $t^* = 65.11$, (c) $t^* = 65.22$, (d) $t^* = 66.66$, (e) $t^* = 71.42$, (f) $t^* = 73.78$, (g) $t^* = 76.81$.

From the spatio-temporal diagram, figure 18, it is also possible to determine the capillary wave celerity. However, different capillary waves do not propagate at the same speed. Waves with smaller wavelength closer to the middle of the satellite lobe have higher velocities than larger waves nearer to the plug foot. This is consistent with the classical expression of inertial capillary waves

$$c = \sqrt{\frac{\sigma}{\rho_l} k \tan kh} \approx \sqrt{\frac{\sigma h}{\rho_l}} k. \quad (7.2)$$

Moreover, the orders of magnitudes ranging from 0.45 m s^{-1} to 1 m s^{-1} are in a good agreement with such a model. An inertial process may thus explain the transport of these capillary waves, although viscous effects may also play a role, as in the capillary ripples preceding an advancing meniscus (Bretherton 1961; Dietze 2016).

The propagation and viscous dissipation of capillary waves at the plug foot helps to explain the aftershocks in figure 17. In particular, the first aftershock is simultaneous with a strong thinning of the film close to the plug foot. This aftershock is higher than the initial peak corresponding to the occlusion. Subsequent aftershocks seem to be linked to the capillary wave dissipation and reflection on the plug foot. This phenomenon highlights the importance of both the convective/inertial and the viscous contributions to the Navier–Stokes equations after the plug formation, as the former are responsible for the wave formation after channel occlusion and to their propagation along the interface while the latter attenuates the capillary waves. A major effect of these capillary waves is a quick film thinning at the plug foot that was observed to be much more gradual in the validation case from § 4.2, where inertia was negligible and capillary waves non-existent.

As a conclusion, we note that inertial and convective contributions appear to dominate the nonlinear channel occlusion phenomenon both when considering time scales (§ 7.3.1) and capillary waves (§ 7.3.2). However, the viscous contribution is essential for plug formation in thick films.

8. Conclusion

In this study we have examined the role played by inertia and viscosity effects on the dynamics of the Plateau–Rayleigh instability in a cylindrical capillary. The numerical results are obtained mainly for liquid water as the outer fluid and water vapour as the core fluid, which is representative of fuel cell applications. We used as a reference a DNS approach, based on a front-tracking algorithm validated on previous analytical, experimental and numerical works. It includes all the terms of the Navier–Stokes equations. A nonlinear lubrication model has also been developed. It extends that of Gauglitz & Radke (1988) by including the core fluid and the cylindrical symmetry. Finally, *ad hoc* models including either viscosity, inertia or both contributions have been developed in a linear approximation.

A linear stability analysis has been performed by comparing these models to the DNS and to the lubrication model, leading to the following conclusions. (a) The existence of an inertial regime for thick films has been evidenced. The transition between the viscous regime, well approximated by the lubrication theory, and the inertial regime is observed for a dimensionless unperturbed film thickness ϵ close to 0.2 for the water/vapour fluid combination used in our application. Both regimes should be present for any fluid and the transition threshold should depend on the fluid properties. (b) The presence of a core fluid slows the instability development; this effect grows with the film thickness if the core fluid viscosity is important. The core fluid does not affect the instability growth rate in the opposite case. Hence, as thick films are ruled by the inertial regime, the effects of the core gas are negligible in fuel cell conditions, without an imposed core gas flow. (c) In the viscous regime, the assumptions of the lubrication approach are verified; the lubrication results for thin films perfectly match the growth rates obtained from DNS and more complete models.

The contributions of inertia, convection and viscosity to the pressure gradient have been evaluated inside and outside the linear regime. The results from the linear stability analysis have been verified. The transition between the inertial and viscous regimes can

be interpreted as a transition in the nature of the transport of the kinetic energy from the interface (where it is generated by capillarity) to the wall (where it is dissipated by viscous friction). In the viscous regime the energy is transported by viscous diffusion, while in the inertial regime it is transported by inertia. For thin films, the conclusions of the linear stability analysis persist outside the linear regime. All phenomena related to the stabilisation of the main collars and to the formation of the satellite lobes, their drainage and motion can be explained by considering only viscous and capillary forces. For these cases, the results of our lubrication model match those of the DNS. Using a lubrication approach and neglecting inertia appears reasonable. Nevertheless, inertial and convective contributions to the pressure gradient become dominant for thicker films.

In summary, with the notable exception of thin films that are entirely governed by the balance between viscous and surface tension forces, inertia is essential to capture and model the development of the Plateau–Rayleigh instability in capillaries, for liquid/vapour water systems. The growth of the instability is dominated by inertia in thick films, both inside and outside the linear regime. In intermediate films, albeit not being dominant it can not be neglected. Lastly, inertia governs the nonlinear formation of plugs: its value soars at the tips of the rising collar in the few instants preceding channel occlusion, leading to the formation of capillary waves. These waves propagate along the plug edges towards the wall and then on the satellite lobes. Nevertheless, even in thick films, viscous forces must be considered in addition to inertia as they explain the dissipation of these waves.

Beyond demonstrating the key role of inertia in fuel cell conditions, this study also emphasises the possibilities offered by the combined use of analytical and numerical methods. It is also noted that in the context of actual fuel cell channels, one cannot avoid using DNS due to the complexity of the system. Analytical models can nevertheless be useful to simulate the long-time behaviour of thin films, where DNS would require considerable computation time and fine meshing.

In future works the effects of an external core flow on the plug formation phenomenon, and notably the conditions where it is inhibited, will be investigated. The complementary use of DNS and analytical models to approach realistic fuel cell conditions will also be pursued. Finally, the results obtained at a single-channel level must be scaled up to be used at the fuel cell scale.

Supplementary movies. Supplementary movies are available at <https://doi.org/10.1017/jfm.2024.1024>.

Acknowledgements. The authors are grateful to G. Dietze for fruitful discussions.

Funding. M.R. acknowledges the CEA PhD scholarship attributed in the framework of the CFR programme.

Declaration of interest. The authors report no conflict of interest.

Author ORCIDs.

 Elie Saikali <https://orcid.org/0000-0002-3525-7063>;

 Vadim S. Nikolayev <https://orcid.org/0000-0002-9486-746X>.

Appendix A. Derivation of the lubrication model

Introducing (5.10) into (5.11) leads to a differential equation on v_z that can be easily solved to obtain the radial profile of v_z in each fluid. Introducing the boundary conditions and

assuming $\partial_r v_z(r=0) = 0$, one gets

$$v_{z,l}(r, z) = \frac{1}{4\mu_l} \left[\frac{\partial p_l}{\partial z} (r^2 - R_0^2) + 2 \left(\frac{\partial p_g}{\partial z} - \frac{\partial p_l}{\partial z} \right) R_i^2 \ln \left(\frac{r}{R_0} \right) \right], \quad (A1)$$

$$v_{z,g}(r, z) = \frac{1}{4\mu_g} \frac{\partial p_g}{\partial z} (r^2 - R_i^2) + \frac{1}{4\mu_l} \frac{\partial p_l}{\partial z} (R_i^2 - R_0^2) + \frac{1}{2\mu_l} \left(\frac{\partial p_g}{\partial z} - \frac{\partial p_l}{\partial z} \right) R_i^2 \ln \left(\frac{R_i}{R_0} \right). \quad (A2)$$

Integrating along r between 0 and R_i for the gas and R_i and R_0 for the liquid, and using the pressure jump boundary condition (5.12) gives the flow rates in each phase:

$$Q_l = A \frac{\partial p_g}{\partial z} + B\sigma \frac{\partial \kappa}{\partial z}, \quad (A3)$$

$$Q_g = C \frac{\partial p_g}{\partial z} + D\sigma \frac{\partial \kappa}{\partial z}. \quad (A4)$$

Here A, B, C and D are coefficients depending on h only:

$$A = -\frac{\pi}{8\mu_l} (R_0^2 - R_i^2)^2, \quad (A5)$$

$$B = -\frac{\pi}{8\mu_l} \left[(R_0^2 - R_i^2)(3R_i^2 - R_0^2) + 4R_i^4 \ln \left(\frac{R_i}{R_0} \right) \right], \quad (A6)$$

$$C = -\frac{\pi}{4\mu_l} R_i^2 \left[R_i^2 \left(\frac{1}{2m} - 1 \right) + R_0^2 \right], \quad (A7)$$

$$D = \frac{\pi}{4\mu_l} R_i^2 \left[2R_i^2 \ln \left(\frac{R_i}{R_0} \right) + R_0^2 - R_i^2 \right]. \quad (A8)$$

Using the conservation of volume in the tube ((5.6) and (5.7)), $\partial_z p_g$ can be eliminated in the flow rate expressions (A3) and (A4). Finally, (5.8) leads to

$$-2\pi R_i \frac{\partial h}{\partial t} = \frac{\partial Q_l}{\partial z} = \sigma \frac{\partial}{\partial z} \left\{ \left[B - \frac{A(B+D)}{A+C} \right] \left(\frac{\partial^3 h}{\partial z^3} + \frac{1}{R_i^2} \frac{\partial h}{\partial z} \right) \right\}, \quad (A9)$$

which is (5.14) with $\beta = B - A(B+D)/(A+C)$.

Appendix B. Derivation of the dispersion models

B.1. General case

In the case where both inertia and viscosity are considered, solving (5.25) gives the streamfunction expressions in each fluid, i.e.

$$\psi_g = [C_g I_1(kr) + D_g I_1(k_g r)] r \exp(i\omega t + ikz), \quad (B1)$$

$$\psi_l = [A_l K_1(kr) + B_l K_1(k_l r) + C_l I_1(kr) + D_l I_1(k_l r)] r \exp(i\omega t + ikz), \quad (B2)$$

where six integration constants A_l, B_l, C_l, D_l need to be determined. The finiteness of velocities for $r \rightarrow 0$ leads to the absence of K_1 functions in ψ_g . The velocities are then

derived from (5.21a,b):

$$v_{r,g} = ik[C_g I_1(kr) + D_g I_1(k_g r)] \exp(i\omega t + ikz), \tag{B3}$$

$$v_{z,g} = -k \left[C_g I_0(kr) + D_g \frac{k_g}{k} I_0(k_g r) \right] \exp(i\omega t + ikz), \tag{B4}$$

$$v_{r,l} = ik[A_l K_1(kr) + B_l K_1(k_l r) + C_l I_1(kr) + D_l I_1(k_l r)] \exp(i\omega t + ikz), \tag{B5}$$

$$v_{z,l} = -k \left[-A_l K_0(kr) - B_l \frac{k_l}{k} K_0(k_l r) + C_l I_0(kr) + D_l \frac{k_l}{k} I_0(k_l r) \right] \exp(i\omega t + ikz). \tag{B6}$$

The no-slip boundary condition (two equations), the velocity continuity at the interface (5.4) (two equations) and the tangential stress continuity (5.26) lead respectively to

$$\left. \begin{aligned} 0 &= A_l K_1(ax) + B_l K_1(ax_l) + C_l I_1(ax) + D_l I_1(ax_l), \\ 0 &= -A_l K_0(ax) - B_l \frac{x_l}{x} K_0(ax_l) + C_l I_0(ax) + D_l \frac{x_l}{x} I_0(ax_l), \\ C_g I_1(x) + D_g I_1(x_g) &= A_l K_1(x) + B_l K_1(x_l) + C_l I_1(x) + D_l I_1(x_l), \\ C_g I_0(x) + D_g \frac{x_g}{x} I_0(x_g) &= -A_l K_0(x) - B_l \frac{x_l}{x} K_0(x_l) + C_l I_0(x) + D_l \frac{x_l}{x} I_0(x_l), \\ 2mC_g I_1(x) + mD_g \frac{x_g^2 + x^2}{x^2} I_1(x_g) &= 2A_l K_1(x) + B_l \frac{x_l^2 + x^2}{x^2} K_1(x_l) \\ &\quad + 2C_l I_1(x) + D_l \frac{x_l^2 + x^2}{x^2} I_1(x_l). \end{aligned} \right\} \tag{B7}$$

These equations correspond to the first five rows of **M** in (5.29). The fifth row (tangential stress continuity) is modified by replacing x_l^2 with its value $x^2 - \hat{\omega}J_l$, by dividing it by 2 and by using the third line (v_r continuity) in it.

Substituting v_z with its ψ expression in (5.2) gives

$$\frac{\partial p}{\partial z} = i\omega \frac{\rho}{r} \frac{\partial \psi}{\partial r} + \mu \left(\frac{\partial^2}{\partial r^2} + \frac{1}{r} \frac{\partial}{\partial r} + \frac{\partial^2}{\partial z^2} \right) \left(-\frac{1}{r} \frac{\partial \psi}{\partial r} \right) = i\omega \frac{\rho}{r} \frac{\partial \psi}{\partial r} + \frac{\mu}{r} \frac{\partial}{\partial r} D\psi. \tag{B8}$$

It can then be introduced in the derivative of (5.27) with respect to z to obtain the left-hand side of (5.28). The right-hand side is obtained by replacing h with (5.16), leading to

$$\left[-i\omega \frac{\rho}{r} \frac{\partial \psi}{\partial r} + \frac{\mu}{r} \frac{\partial}{\partial r} D\psi + 2ik\mu \frac{\partial v_r}{\partial r} \right] = -ik\sigma \frac{(kR_i)^2 - 1}{R_i^2} A_0 \exp(i\omega t + ikz). \tag{B9}$$

Equation (5.8) allows us to replace A_0 in (B9), thus obtaining (5.28). After replacement of ψ and v_r with their values, one finally gets the equation

$$\begin{aligned} &\left(2x^2 mI_1'(x) - \hat{\omega}J_g I_0(x) - x \frac{x^2 - 1}{\hat{\omega}} I_1(x) \right) C_g + \left(2x_g x mI_1'(x_g) - x \frac{x^2 - 1}{\hat{\omega}} I_1(x_g) \right) D_g \\ &= (2x^2 K_1'(x) + \hat{\omega}J_l K_0(x)) A_l + 2x_l x K_1'(x_l) B_l \\ &\quad + (2x^2 I_1'(x) - \hat{\omega}J_l I_0(x)) C_l + 2x_l x I_1'(x_l) D_l, \end{aligned} \tag{B10}$$

which, after an appropriate addition of the third and fourth lines of the set (B7), gives the last row of the matrix (5.29).

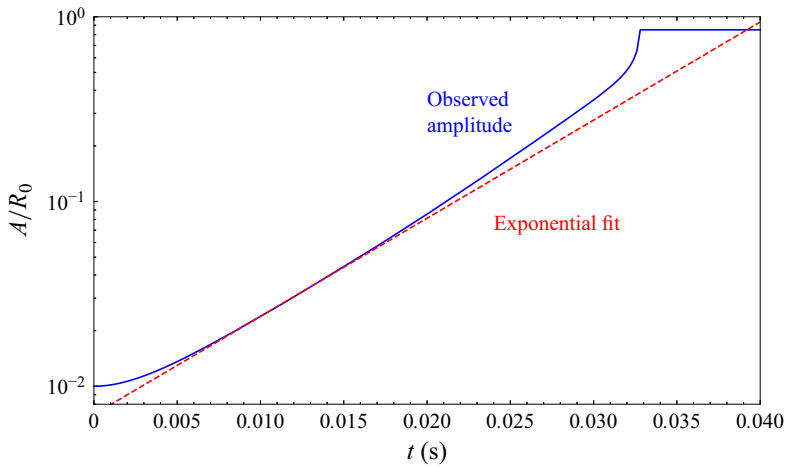


Figure 19. Evolution of the maximum amplitude of the film over time for a film of initial thickness $\epsilon = 0.15$ and a wavelength $\lambda = 4.44$ mm close to the maximum growth rate of the instability. This corresponds to the simulation from figure 4(c,d). The vertical axis is in semi-log scale so the exponential fit is a straight line, the slope of which gives the growth rate ω_i^{-1} .

B.2. Absence of inertia

The same set of equations is used to obtain \mathbf{M} in (5.32). The only difference is that ψ is replaced by its degenerated value at small densities:

$$\psi_g = [C_g I_1(kr) + D_g kr I_0(kr)] r \exp(i\omega t + ikz), \tag{B11}$$

$$\psi_l = [A_l K_1(kr) + B_l kr K_0(kr) + C_l I_1(kr) + D_l kr I_0(kr)] r \exp(i\omega t + ikz). \tag{B12}$$

Appendix C. Determination of the growth rate in the linear regime of DNS

The growth rates from DNS are determined as follows. First, the maximum amplitude A of the film height in the central part of the simulation domain is plotted over time. Only the central part is considered to avoid the impact of lateral boundary conditions. Indeed, as can be observed in figure 4, liquid bulges are present close to the lateral domain boundaries. They are caused by the fixed film interface boundary conditions.

Figure 19 provides an example of the evolution of A for the case in figure 4(c,d). After a transient, the instability reaches a zone where the amplitude evolution is exponential with a characteristic time ω_i^{-1} . An exponential fit (in red in figure 19) is performed in the time zone where the amplitude is between $0.02R_0$ and $0.04R_0$. This ensures that the flow is well developed and that the instability is still in its linear regime. The transient zone preceding the linear zone is due to the initial conditions that do not correspond to the linear regime solution requiring a proportionality of perturbations of all the variables. On the contrary, in the DNS, the initial perturbations of all the variables are zero except the film deformation A . The slope of the fitting line gives the destabilisation time ω_i^{-1} . The time zone is then manually varied to obtain an estimate of the uncertainty linked to ω_i . These uncertainties, due to the initial transient zone, are reported in figure 10.

REFERENCES

AUL, R.W. & OLBRICHT, W.L. 1990 Stability of a thin annular film in pressure-driven, low-Reynolds-number flow through a capillary. *J. Fluid Mech.* **215**, 585.

Plateau–Rayleigh instability in a capillary

- BELL, I.H., WRONSKI, J., QUOILIN, S. & LEMORT, V. 2014 Pure and pseudo-pure fluid thermophysical property evaluation and the open-source thermophysical property library coolprop. *Ind. Engng Chem. Res.* **53**, 2498–2508.
- BERESNEV, I.A., LI, W. & VIGIL, R.D. 2009 Condition for break-up of non-wetting fluids in sinusoidally constricted capillary channels. *Transp. Porous Med.* **80**, 581–604.
- BIAN, S., TAI, C.-F., HALPERN, D., ZHENG, Y. & GROTBORG, J.B. 2010 Experimental study of flow fields in an airway closure model. *J. Fluid Mech.* **647**, 391–402.
- BRETHERTON, F.P. 1961 The motion of long bubbles in tubes. *J. Fluid Mech.* **10**, 166.
- CALVIN, C., CUETO, O. & EMONOT, P. 2002 An object-oriented approach to the design of fluid mechanics software. *Math. Modelling Numer. Anal.* **36**, 907–921.
- CAMASSA, R., OGROSKY, H.R. & OLANDER, J. 2014 Viscous film flow coating the interior of a vertical tube. Part 1. Gravity-driven flow. *J. Fluid Mech.* **745**, 682–715.
- CAMASSA, R., OGROSKY, H.R. & OLANDER, J. 2017 Viscous film-flow coating the interior of a vertical tube. Part 2. Air-driven flow. *J. Fluid Mech.* **825**, 1056–1090.
- CHEAH, M.J., KEVREKIDIS, I.G. & BENZIGER, J.B. 2013 Water slug formation and motion in gas flow channels: the effects of geometry, surface wettability, and gravity. *Langmuir* **29** (31), 9918–9934.
- CHRISTIANSEN, R.M. & HIXSON, A.N. 1957 Breakup of a liquid in a denser liquid. *Ind. Engng Chem.* **49**, 1017–1024.
- DU CLUZEAU, A., BOIS, G. & TOUTANT, A. 2019 Analysis and modelling of Reynolds stresses in turbulent bubbly up-flows from direct numerical simulations. *J. Fluid Mech.* **866**, 132–168.
- DENG, W., CARDENAS, M.B. & BENNETT, P.C. 2014 Extended roof snap-off for a continuous nonwetting fluid and an example case for supercritical CO₂. *Adv. Water Resour.* **64**, 34–46.
- DIETZE, G.F. 2016 On the Kapitza instability and the generation of capillary waves. *J. Fluid Mech.* **789**, 368–401.
- DIETZE, G.F., PICARDO, J.R. & NARAYANAN, R. 2018 Sliding instability of draining fluid films. *J. Fluid Mech.* **857**, 111–141.
- DIETZE, G.F. & RUYER-QUIL, C. 2015 Films in narrow tubes. *J. Fluid Mech.* **762**, 68–109.
- EGGERS, J. & DUPONT, T.F. 1994 Drop formation in a one-dimensional approximation of the Navier–Stokes equation. *J. Fluid Mech.* **262**, 205–221.
- EGGERS, J. & VILLERMAUX, E. 2008 Physics of liquid jets. *Rep. Prog. Phys.* **71**, 036601.
- ERKEN, O., FAZLA, B., MURADOGLU, M., IZBASSAROV, D., ROMANÒ, F. & GROTBORG, J.B. 2023 Effects of elastoviscoplastic properties of mucus on airway closure in healthy and pathological conditions. *Phys. Rev. Fluids* **8**, 053102.
- EVERETT, D.H. & HAYNES, J.M. 1972 Model studies of capillary condensation. I. Cylindrical pore model with zero contact angle. *J. Colloid Interface Sci.* **38**, 125–137.
- FRENKEL, A.L., BABCHIN, A.J., LEVICH, B.G., SHLANG, T. & SIVASHINSKY, G.I. 1987 Annular flows can keep unstable films from breakup: nonlinear saturation of capillary instability. *J. Colloid Interface Sci.* **115**, 225–233.
- FUJIOKA, H. & GROTBORG, J.B. 2004 Steady propagation of a liquid plug in a two-dimensional channel. *Trans. ASME J. Biomech. Engng* **126**, 567–577.
- GAUGLITZ, P.A. & RADKE, C.J. 1988 An extended evolution equation for liquid film breakup in cylindrical capillaries. *Chem. Engng Sci.* **43**, 1457–1465.
- GAUGLITZ, P.A. & RADKE, C.J. 1990 The dynamics of liquid film breakup in constricted cylindrical capillaries. *J. Colloid Interface Sci.* **134**, 14–40.
- GEORGIU, E., PAPAGEORGIU, D.T., MALDARELLI, C. & RUMSCHITZKI, D.S. 1991 The double layer-capillary stability of an annular electrolyte fluid surrounding a dielectric-fluid core in a tube. *J. Fluid Mech.* **226**, 149–174.
- GOLDSMITH, H.L. & MASON, S.G. 1963 The flow of suspensions through tubes. II. Single large bubbles. *J. Colloid Sci.* **18**, 237–261.
- GOREN, S.L. 1962 The instability of an annular thread of fluid. *J. Fluid Mech.* **12** (2), 309–319.
- GOYENECHÉ, M., LASSEUX, D. & BRUNEAU, D. 2002 A film-flow model to describe free water transport during drying of a hygroscopic capillary porous medium. *Transp. Porous Med.* **48**, 125–158.
- GÜNTHER, A., KHAN, S.A., THALMANN, M., TRACHSEL, F. & JENSEN, K.F. 2004 Transport and reaction in microscale segmented gas-liquid flow. *Lab on a Chip* **4**, 278–286.
- HAGEDORN, J.G., MARTYS, N.S. & DOUGLAS, J.F. 2004 Breakup of a fluid thread in a confined geometry: droplet-plug transition, perturbation sensitivity, and kinetic stabilization with confinement. *Phys. Rev.* **69**, 056312.
- HALPERN, D., FUJIOKA, H., TAKAYAMA, S. & GROTBORG, J.B. 2008 Liquid and surfactant delivery into pulmonary airways. *Respir. Physiol. Neurobiol.* **163**, 222–231.

- HALPERN, D. & GROTBORG, J.B. 1992 Fluid-elastic instabilities of liquid-lined flexible tubes. *J. Fluid Mech.* **244**, 615.
- HALPERN, D. & GROTBORG, J.B. 2003 Nonlinear saturation of the Rayleigh instability due to oscillatory flow in a liquid-lined tube. *J. Fluid Mech.* **492**, 251–270.
- HALPERN, D., JENSEN, O.E. & GROTBORG, J.B. 1998 A theoretical study of surfactant and liquid delivery into the lung. *J. Appl. Physiol.* **85**, 333–352.
- HAMMOND, P.S. 1983 Nonlinear adjustment of a thin annular film of viscous fluid surrounding a thread of another within a circular cylindrical pipe. *J. Fluid Mech.* **137**, 363–384.
- HAZEL, A.L. & HEIL, M. 2005 Surface-tension-induced buckling of liquid-lined elastic tubes: a model for pulmonary airway closure. *Proc. R. Soc.* **461**, 1847–1868.
- HICKOX, C.E. 1971 Instability due to viscosity and density stratification in axisymmetric pipe flow. *Phys. Fluids* **14**, 251–262.
- HUSSAINI, I.S. & WANG, C.-Y. 2009 Visualization and quantification of cathode channel flooding in PEM fuel cells. *J. Power Sources* **187**, 444–451.
- JOHNSON, M., KAMM, R.D., HO, L.W., SHAPIRO, A. & PEDLEY, T.J. 1991 The nonlinear growth of surface-tension-driven instabilities of a thin annular film. *J. Fluid Mech.* **233**, 141–156.
- KATAOKA, I. 1986 Local instant formulation of two-phase flow. *Intl J. Multiphase Flow* **12**, 745–758.
- KERCHMAN, V. 1995 Strongly nonlinear interfacial dynamics in core-annular flows. *J. Fluid Mech.* **290**, 131–166.
- LEE, W.-K. & FLUMERFELT, R.W. 1981 Instability of stationary and uniformly moving cylindrical fluid bodies-I. Newtonian systems. *Intl J. Multiphase Flow* **7**, 363–383.
- LIAO, Y.-C., LI, Y.-C. & WEI, H.-H. 2013 Drastic changes in interfacial hydrodynamics due to wall slippage: slip-intensified film thinning, drop spreading, and capillary instability. *Phys. Rev. Lett.* **111**, 136001.
- LISTER, J.R., RALLISON, J.M., KING, A.A., CUMMINGS, L.J. & JENSEN, O.E. 2006a Capillary drainage of an annular film: the dynamics of collars and lobes. *J. Fluid Mech.* **552**, 311.
- LISTER, J.R., RALLISON, J.M. & REES, S.J. 2006b The nonlinear dynamics of pendent drops on a thin film coating the underside of a ceiling. *J. Fluid Mech.* **647**, 239–264.
- LU, Z., RATH, C., ZHANG, G. & KANDLIKAR, S.G. 2011 Water management studies in pem fuel cells, part IV: effects of channel surface wettability, geometry and orientation on the two-phase flow in parallel gas channels. *Intl J. Hydrogen Energy* **36**, 9864–9875.
- MAGNINI, M. 2022 Bubbles in capillaries: relaxing traditional assumptions. *Sci. Talks* **2**, 100020.
- MAGNINI, M., FERRARI, A., THOME, J.R. & STONE, H.A. 2017 Undulations on the surface of elongated bubbles in confined gas-liquid flows. *Phys. Rev. Fluids* **2**, 084001.
- MATHIEU, B. 2003 Etudes physiques, expérimentale et numérique des mécanismes de base intervenant dans les écoulements diphasiques. PhD thesis, Université de Provence, Polytech Marseille.
- NEWHOUSE, L.A. & POZRIKIDIS, C. 1992 The capillary instability of annular layers and liquid threads. *J. Fluid Mech.* **242**, 193–209.
- PAPAGEORGIOU, D.T., MALDARELLI, C. & RUMSCHITZKI, D.S. 1990 Nonlinear interfacial stability of core-annular film flows. *Phys. Fluids* **2**, 340–352.
- PETSC 2024 Portable, extensible toolkit for scientific computation (PETSC) library. Available at: <https://www.mcs.anl.gov/petsc/>.
- PLATEAU, J.A.F. 1873 Statique Expérimentale Et Théorique Des Liquides Soumis Aux Seules Forces Moléculaires, vol. 1. Gauthiers-Villars.
- RAYLEIGH, LORD 1878 On the instability of jets. *Proc. Lond. Math. Soc.* **s1-10**, 4–13.
- ROMANÒ, F., FUJIOKA, H., MURADOGLU, M. & GROTBORG, J.B. 2019 Liquid plug formation in an airway closure model. *Phys. Rev. Fluids* **4** (9), 093103.
- ROMANÒ, F., MURADOGLU, M., FUJIOKA, H. & GROTBORG, J.B. 2021 The effect of viscoelasticity in an airway closure model. *J. Fluid Mech.* **913**, A31.
- ROMANÒ, F., MURADOGLU, M. & GROTBORG, J.B. 2022 Effect of surfactant in an airway closure model. *Phys. Rev. Fluids* **7**, 093103.
- ROSENZWEIG, J. & JENSEN, O.E. 2002 Capillary-elastic instabilities of liquid-lined lung airways. *Trans. ASME J. Biomech. Engng* **124**, 650–655.
- RUYER-QUIL, C. & MANNEVILLE, P. 2002 Further accuracy and convergence results on the modeling of flows down inclined planes by weighted-residual approximations. *Phys. Fluids* **14**, 170–183.
- SAAD, Y. 2003 *Iterative Methods for Sparse Linear Systems*. SIAM.
- SAIKALI, E. 2018 Numerical modelling of an air-helium buoyant jet in a two vented enclosure. PhD thesis, Sorbonne Université.
- SAIKALI, E., LEDAC, P., BRUNETON, A., KHIZAR, A., BOURCIER, C., BERNARD-MICHEL, G., ADAM, E. & HOUSSIN-AGBOMSON, D. 2021 Numerical modeling of a moderate hydrogen leakage in

Plateau–Rayleigh instability in a capillary

- a typical two-vented fuel cell configuration. International Conference on Hydrogen Safety (ICHS 2021). cea-04411171.
- TAI, C.-F., BIAN, S., HALPERN, D., ZHENG, Y., FILOCHE, M. & GROTBORG, J.B. 2011 Numerical study of flow fields in an airway closure model. *J. Fluid Mech.* **677**, 483–502.
- TJAHJADI, M., STONE, H.A. & OTTINO, J.M. 1992 Satellite and subsatellite formation in capillary breakup. *J. Fluid Mech.* **243**, 297.
- TOMOTIKA, S. 1935 On the instability of a cylindrical thread of a viscous liquid surrounded by another viscous fluid. *Proc. R. Soc.* **150**, 322–337.
- WEBER, C. 1931 Zum zerfall eines flüssigkeitsstrahles. *Z. Angew. Math. Mech.* **11**, 136–154.
- ZHAO, C., ZHANG, Y. & SI, T. 2023 Slip-enhanced Rayleigh–Plateau instability of a liquid film on a fibre. *J. Fluid Mech.* **954**, A46.